Graduation Thesis

Study on Slope Estimation of Planetary Surface Using Shape from Shading

(Shape from Shading法を用いた天体表面の斜面推定に関する研究)

2019.08.08

Supervisor: Prof. Hashimto Tatsuaki

Department of Electrical Engineering and Information Systems
Graduate School of Engineering
The University of Tokyo

Master Course
37-175076
Di Mengzhi

Contents

List of Figures

List of Tables

1 Introduction

1.1 Background

Since the Soviet Union launched Luna 1 in 1959, space exploration activities have been carried out for 60 years. In order to clarify the origin and evolution of the earth, research for extraterrestrial resources, and expand the scope of human activities, many countries have been actively promoted space development and carried out various space exploration missions during these 60 years. The timeline for space exploration missions is shown in Figure 1.

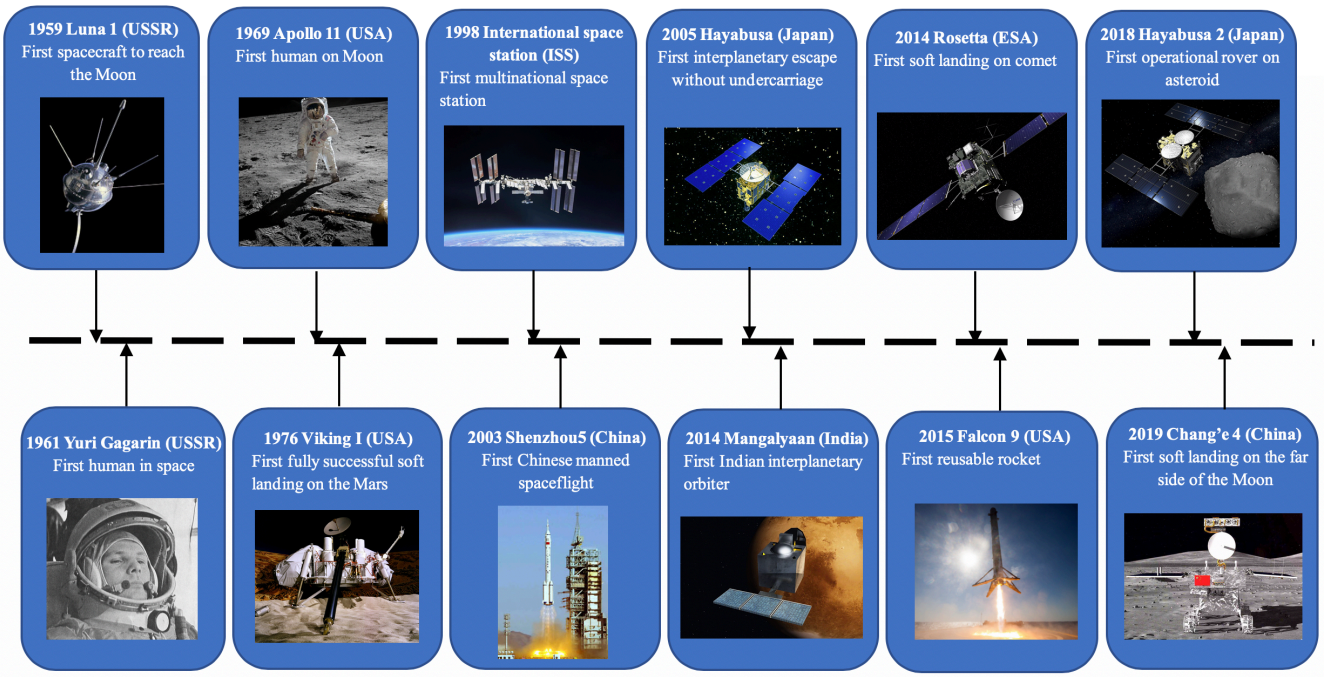

Figure 1. Timeline for space exploration missions

According to this timeline, it can be seen that as the scientific return requirements for space exploration missions increase, landing missions, sample return and manned landing have become one of the most important parts of deep space exploration activities. And the safe landing of the spacecraft on the surface of target planet is a

prerequisite to ensure smooth implementation of the above-mentioned exploration activities.

To date, many countries have already carried out various landing missions. In order to ensure a high landing success rate, most of the spacecrafts chose relatively flat areas with fewer obstacles as landing site. However, many target points with high scientific value are located close to dangerous areas, such as the edge of crater, rugged mountains. These places are often considered as hazardous areas and excluded from possible landing site selection, which largely sacrifices the scientific value of the exploration missions. For example, the Mars Exploration Rovers mission selected Gusev Crater and Meridiani Planum rather than other higher scientifically interesting areas for the reason that they are flat plains which are relatively free of landing hazards [1]. As human exploration of space continues, more and more complex terrains (areas around rocks, craters, and steep slopes) will be included in the scientific investigations. In order to achieve a safe landing on complex areas that are scientifically interesting but hazardous, and increase the scientific return of exploration activities, future interplanetary landers are required to have high-precision obstacle detection and avoidance capability.

Also, when exploring the extraterrestrial planets, since the spacecraft is far away from the earth, there is large communication delay between the spacecraft and the ground monitoring center. The traditional navigation guidance method based on the deep space network tracking cannot satisfy the real-time navigation requirement. Thus the spacecraft is required to have some functions to detect and avoid obstacles autonomously.

Therefore, conducting research on obstacle detection and avoidance technology for landing has become one of the most important research topics for space exploration field in recent years.

1.2 Obstacle avoidance and landing site selection for landing missions in recent years

Since 1960s, various countries have launched multiple lunar and Mars landing spacecrafts. For the early lunar landing missions, limited to the technical level at that

time, the Luna program and the Surveyor program did not have autonomous obstacle recognition and avoidance capabilities, resulting in a low landing success rate. The Apollo program achieved successful landing through manual control, astronauts observed the planetary surface and manipulated the control system to achieve obstacle avoidance and safe landing. And for Mars, most of the early Mars landers used airbag landing to resolve obstacle avoidance problem.

In recent years, most spacecrafts conducted landing missions through choosing candidate landing areas in advance by researchers, then detecting obstacles and finding proper landing site within this chosen landing areas autonomously. For example, the Chang'e 3 (Figure 2), after selecting the Sinus Iridum as candidate landing zone, it completed obstacle detection and avoidance autonomously, and successfully touched down at 19.51256°W and 44.11884°N in the east of Sinus Iridum [2]. The soft landing process of Chang'e-3 lander is shown in Figure 3, it can be divided into seven phases: (1) preparation for landing, (2) primary deceleration, (3) quick adjusting, (4) approaching, (5) hovering, (6) hazard avoidance, (7) constant low velocity descent [3]. (4) — (7) phases are obstacle avoidance process, they completed the functions of coarse obstacle detection, precise obstacle detection, precision obstacle avoidance and constant low velocity descent, respectively.

(1) Preparation for landing phase corrected the ignition time and the corresponding orbit, calculated the ignition target attitude and adjust it in place before powered descent.

(2) Primary deceleration phase was the first sub-phase for powered descent. The lander descended from ~15km to ~3km above the lunar surface.

(3) Quick adjusting phase seamlessly connected the primary deceleration phase and approaching phase. The lander descended from ~3km to ~2.4km above the lunar surface.

(4) Approaching phase: The main task of this phase was to perform coarse hazard detection and avoidance, in which the lander descended from ~2.4 km to ~100 m. The gray images of the pre-selected landing zone were acquired by the optical imaging sensor, and large obstacles (craters and rocks larger than 1 m in diameter) were identified by image processing methods to determine potential safe landing regions and implement the first obstacle avoidance.

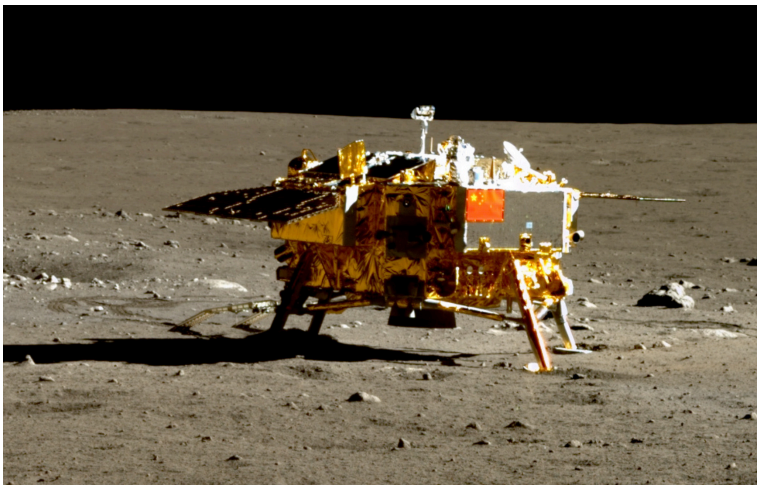

Figure 2. Chang'e 3 lander on lunar surface

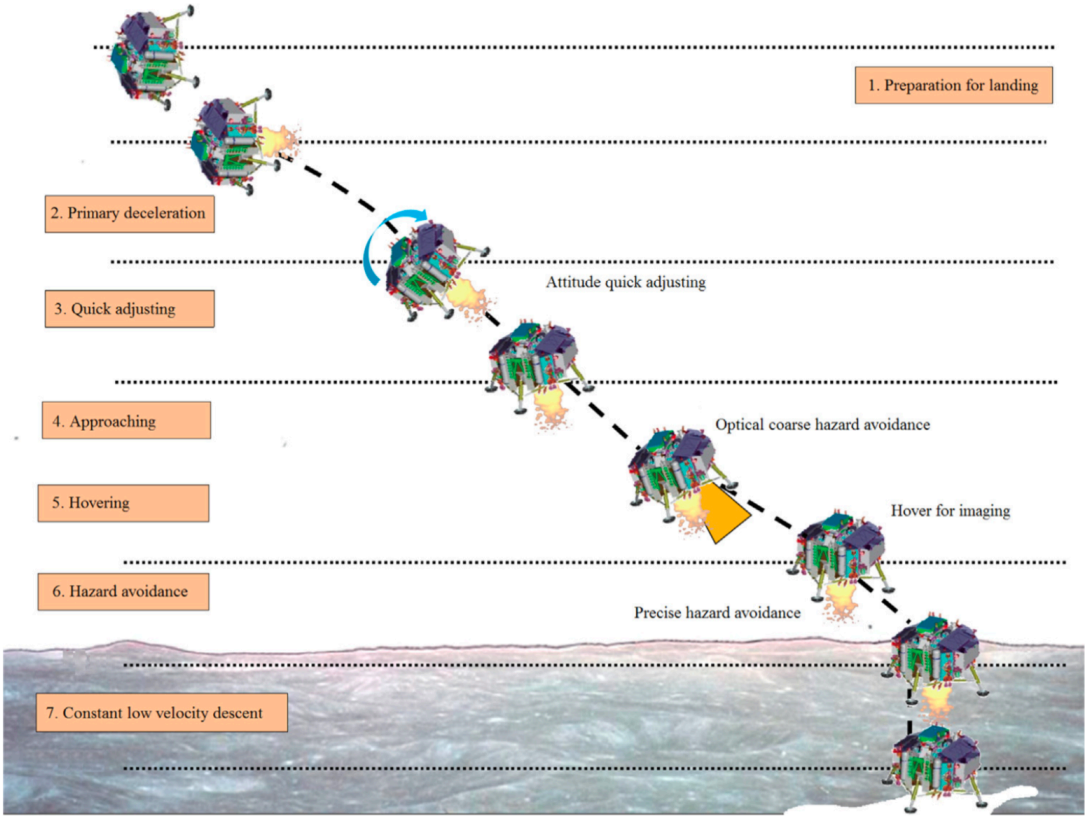

Figure 3. The scheme for Chang'e 3 powered descent and landing

(5) Hovering phase: The lander hovered at ~100 m above the lunar surface. The main task was to perform precise obstacle detection, using laser imaging sensor to obtain the high-precision three-dimensional elevation data of the 50 × 50 m^2 area under

the lander. Then the craters larger than 20 cm and slopes steeper than 8 degrees were detected, and the nearest safe landing site were determined.

(6) Hazard avoidance phase: The lander performed precise hazard avoidance and descent simultaneously. Based on the safe landing site information given by the hovering phase, the lander descends from ~100m to ~30 m above the landing site.

(7) Constant low velocity descent phase: The main task of this phase was to eliminate the horizontal velocity and align the attitude of the lander with the normal direction of the surface without changing the current horizontal position. The lander descended vertically at a constant speed of 2 m/s from ~30 m to ~2m above the landing point.

Chang'e 3 adopted a coarse-precision-relay obstacle detection and avoidance scheme. For the coarse obstacle avoidance phase, the main purpose is to remove large-size obstacles that obviously endanger the safety of landing in the preselected large landing region and provide potential safe landing areas for the following precise avoidance. Since the lander moves at a relatively large velocity at high altitude, the sensor is required to have fast imaging capability, thus the influence of the lander motion on obstacle detection can be minimized. For the precise obstacle detection and avoidance phase, the main purpose is to perform accurate obstacle detection in the potential safe landing areas that are selected by the coarse obstacle avoidance phase. It is required to identify and eliminate the small size obstacles and determine the safe landing site. There is high requirement for the detection accuracy, but no special requirement for imaging time.

The sensors used for these two phases are chosen according to their different functional requirements. In the coarse obstacle avoidance phase, the optical imaging sensor with short exposure time and good adaptability to lander's moving is used to take images of preselected landing region. Then images are processed to detect large obstacles and choose potential safe landing area. In the precision obstacle avoidance phase, the lander is in a hovering state, and the laser imaging sensor with high detection precision is used to obtain the three dimensional digital elevation map of the potential safe landing area, then find out obstacles with small size and determine the landing site.

1.3 Research status for obstacle detection

1.3.1 Obstacles on the planetary surface

Mainly, four types of features, craters, valleys, rocks, and slopes are considered as obstacles on planetary surface, as shown in Figure 4. Steep slopes and valleys may cause the lander to tip over when landing, directly causing the landing mission to fail. The lander may be damaged if it collides with the edge of the craters or rocks during touch down. And if the lander lands in a rugged terrain, the rover may get stuck and not able to carry out their exploration task smoothly, thus the effectiveness of the landing mission will be greatly reduced. Therefore, it is very important to detect the location and size of obstacles for landing missions.

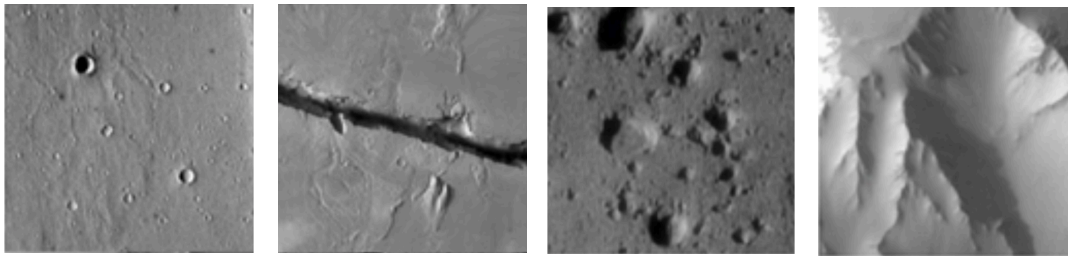

(a) Craters (b) Valleys (c) Rocks (d) Slopes

Figure 4. Obstacles on planetary surface

1.3.2 Previous researches

There are two types of methods for obstacles detection, one is active sensor-based detection methods, the other is passive sensor-based detection methods.

The active sensor is sensor that measures the topography by radiating a certain form of energy (radio waves, light waves, etc.) to the target area and then receiving the reflected energy, such as radar and lidar. This type of sensor measures distance between sensor and targeted terrain. It is able to obtain the three dimensional shape for targeted area, then obtain the obstacle information through data processing which is relatively simple and fast. And it is not constrained by the lighting conditions, it can work under poor illumination such as nighttime. However, the active sensors are expensive, massive, heavy, have high power consumption and narrow field of view.

The passive sensor is sensor that does not radiate any energy to the outside, but indirectly acquires visible or infrared light information reflected by the topography, such as camera. The information that passive sensors obtain is two-dimensional image without depth information, thus it is necessary to either identify features that pose obstacle, or reconstruct three-dimensional topography then obtain obstacle information. Therefore, the calculation is more complicated. And it can only work during daytime. However, compared with active sensors, passive sensors have the advantages of low price, light weight, low power consumption, wider field of view, shorter development cycle, thus they have received a lot of attention.

1.3.3 Passive sensor-based detection methods

The passive sensor-based detection methods can also be subdivided into two options. One is to identify a specific obstacle based on the image characteristics of this type of obstacle. For example, (1) detecting rocks based on the shadow information. Fitting the shadow areas with an ellipse based on the shape characteristics of the rock, then modeling rock as circle according to sun elevation and shadow length to estimate the height and position of the rock [4]. (2) Detecting craters based on template matching. During the orbiting phase, the craters of planetary surface are modeled. Then the detected craters in the image are matched with the craters projected from this previously generated model and best transformation between these two sets is obtained [5]. An important issue with this type of methods is that only certain type of obstacles can be detected because they detect obstacles based on the characteristics of this particular obstacle (for template matching method, if rocks and craters are both modeled in the orbiting phase, both of them can be detected).

The other one is to reconstruct full three-dimensional terrain of the target zone (usually is called digital elevation map), then obtain obstacle information from this reconstructed digital elevation map (DEM). The former approach can only lead to incomplete hazard maps, and it is impossible to judge whether the un-hazardous sites in the detection result are actually safe or not. Therefore, this research only considers the latter one that generates the DEM.

Three methods are often used to reconstruct DEM from images, stereo vision, stereo from motion and shape from shading.

Stereo vision (SV) uses the same principle as the human eye to obtain the distance from the object to the camera as shown in Figure 5. The input is two images (in case of binocular stereo vision) taken from different positions. SV first uses matching operator (eg. the sum of absolute difference operator) as cost function to find the corresponding pixels in two images, this process is called image matching. Then SV obtains disparity map by calculating the difference in image location of these corresponding points. Finally using this disparity map to calculate the distance from the object to the camera by triangulation. In the field of space exploration, the baseline of two cameras is not long considering the limitations of the lander size. In order to achieve high detection accuracy, SV can only be used for obstacle detection at low altitude. According to reference 4, the binocular stereo baseline of ~1 m or more can guarantee high detection accuracy at altitudes up to ~100 m. Reference 6 execute their SV algorithm (supplemented with a parabolic fit for computing non-integer disparity values) at imaging altitudes from 50m to 1000m, and give the conclusion that SV performs well at altitudes below 200 m for a baseline of ~2 m.

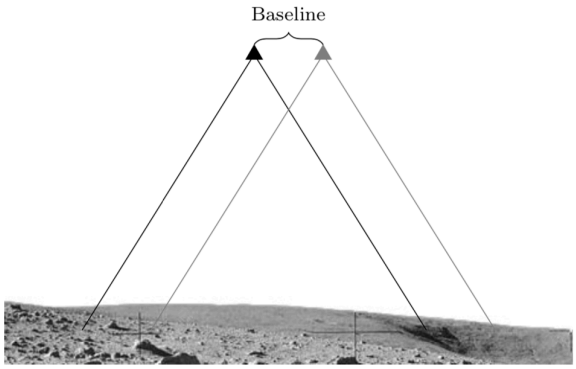

Figure 5. Stereo vision

Structure from motion (SfM) reconstructs DEM based on the motion parallax of a single camera as shown in Figure 6. The input is two (or multiple) images that obtained from the same camera at different time. A set of point features are selected from the first image, then these features are tracked in the second and subsequent images. These corresponding features are used to estimate motion state (position and attitude) of the camera between image acquisitions. Then this motion estimate is used to obtain terrain map through triangulation [7]. Since SfM calculates three-dimensional information based on the motion parallax of a single camera, this method only works well if lander's

trajectory can give adequate parallax, which limits its scope of use. For example, in the final stage of landing, the descent trajectory of lander is almost vertical and the horizontal velocity is very small, SfM cannot work well at this situation. Also, SfM requires very accurate knowledge about spacecraft's state [6], inaccuracies of this prior information will directly lead to errors in the results. Therefore, the implementation of SfM is much more difficult than SV.

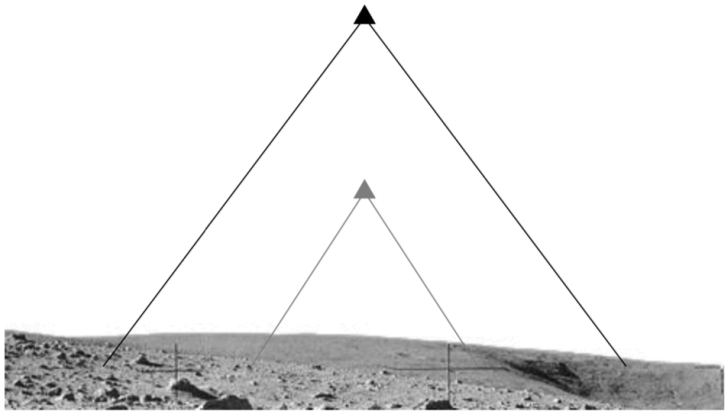

Figure 6. Structure from motion

Shape from Shading (SfS) is a method to derive the surface orientation from the intensity value of image, then reconstruct three dimensional terrain through relationship between surface orientation and depth, as shown in Figure 7. It is based on the fact that the intensity value of given pixel point is uniquely linked to the surface orientation at that point. The input of SfS is a single image. In addition to the input image, the elevation and azimuth of the incoming sunlight have to be known. According to reference 7, at low altitude (within 200m), the detection result of SfS is worse than SV and SfM. But it works well at high altitude, it has no altitude limitation within the altitude range of 2 km.

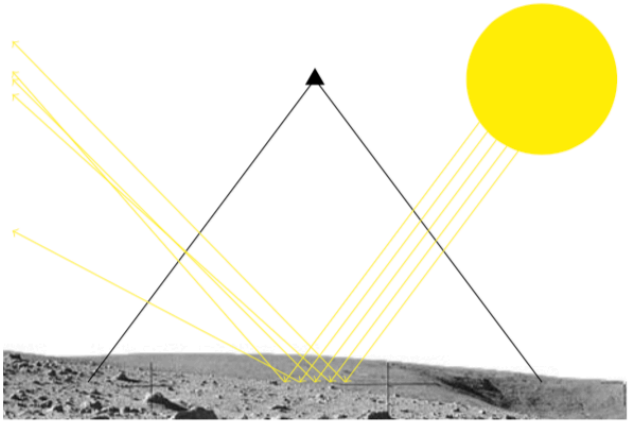

Figure 7. Shape from Shading

1.4 Purpose of this research

As introduced in section 1.3.1, there are mainly four types of obstacles on the planetary surface. Large craters and rocks may damage the landing gear, steep slopes and valleys may cause the lander to fall. In order to ensure a safe landing, the location and size of the obstacles need to be accurately detected during landing. So far, many methods have been proposed to estimate these obstacles. Among them, since the images of craters and rocks have obvious features, there are many related researches. But it is more difficult to detect slopes and there are less studies. This research focuses on the detection of slope surfaces on planetary surface using image processing method.

1.5 Composition of this paper

This paper is divided into five chapters.

The first chapter introduces the background of this research, including the importance of obstacle detection for the space exploration, the way spacecrafts avoid obstacles and find suitable landing site using Chang'e 3 as an example, research status of obstacle detection, the purpose of this research.

The second chapter introduces the Shape from Shading (SfS) method, its principle, four categories of solutions for SfS, the principles and calculation formulas for each method, and the advantages and disadvantages of these four solutions.

The third chapter first tests four SfS methods introduced in the previous chapter

and analyzes their results. Then experiments are carries out using the chosen linear method with Hapke bidirectional reflection model. Detection result is divided into four types of terrains and analyzed separately, then comes to the conclusion that the information provided by single image is not enough to reconstruct the slope surfaces.

The fourth chapter introduces a SfS method combined with low resolution DEM, using single image and corresponding low-resolution DEM as input to reconstruct surface shape. Experimental results show that this method can reconstruct overall terrain and detailed small obstacles.

The fifth chapter is the summary and future work.

2 Shape from shading (SfS)

Three passive sensors-based methods are introduced in Section 1.3.3. Compared with stereo vision and motion stereo, shape from shading has the following advantages: (1) Only a single image is used. (2) No high-precision image matching is required. (3) Imaging altitude has little effect on detection result. Within 2 km altitude, SfS is altitude independent and it is possible to detect obstacles with high accuracy. Therefore, SfS is chosen for this research.

This chapter introduces the principle of SfS, four types of approaches for SfS problem and their advantages and disadvantages.

2.1 Introduction of SfS

Shape from shading (SfS) is a method that uses spatial distribution of image brightness of the target surface to reconstruct the three-dimensional shape of an object. For an actual image, the distribution of brightness is determined by the physical reflection characteristics of the object surface, the position and parameters of the camera (observer), the normal direction of the surface, the illumination conditions, etc. In order to simplify this recovery problem, previous studies have introduced several assumptions: (1) the surface reflection coefficient (albedo) is uniform, (2) the surface is illuminated by a distant point source, (3) imaging geometry is orthogonal projection. To solve SfS problem, it is important to learn how image is formed. A simple model which is often used is Lambert model. This model assumes the surface of the object is a perfect diffusing surface, that the reflection coefficient is constant. The schematic diagram of geometry of this model is shown in Figure 8. Assuming that the reflection coefficient is 1, the intensity of the image is determined only by the angle between the surface normal and the light source direction (referred as incident angle), which is expressed as equation (2.1).

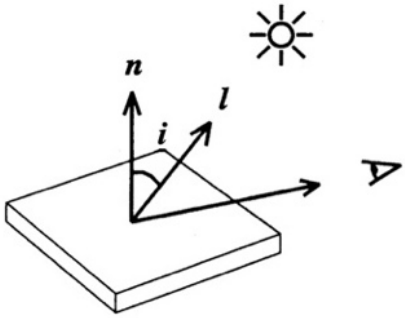

Figure 8. Schematic diagram of geometry of Lambert model

$$I = \cos i \tag{2.1}$$

where I is the intensity value, i is incident angle.

The direction of camera is used as the z-axis to create a coordinate system. For this coordinate system, the surface normal is defined as the orientation of a vector perpendicular to the tangent plane on the object surface. The surface gradients are defined as the rate of change of depth in the x and y directions, respectively. The surface slant is defined as the angle between the surface normal and viewing direction, tilt is defined as the angle between the projection of surface normal on the image plane and the horizontal axis. The relationship between surface depth $z(x, y)$, surface normal $\vec{n} = (n_1, n_2, n_3)$, surface gradient (p, q), surface slant σ and tilt τ are shown as equations (2.2), (2.3) and (2.4).

$$p = \frac{\partial z}{\partial x},\ q = \frac{\partial z}{\partial y} \tag{2.2}$$

$$n_1 = \sin\sigma\cos\tau\,, n_2 = \sin\sigma\sin\tau\,, n_3 = \cos\sigma \tag{2.3}$$

$$p = -\frac{n_1}{n_3}, q = -\frac{n_2}{n_3} \tag{2.4}$$

For light source direction $\vec{L} = (-p_s, -q_s, 1)$ and surface normal $\vec{n} = (-p, -q, 1)$, equation (2.1) can be expressed as a function of (p, q) as follows.

$$I = \frac{\vec{n}\cdot\vec{L}}{|n|\cdot|L|} = \frac{1+pp_s+qq_s}{\sqrt{1+p^2+q^2}\sqrt{1+p_s^2+q_s^2}} = R(p, q) \tag{2.5}$$

This equation is called the image-irradiance equation. Function $R(p, q)$ is referred as reflectance map (as shown in Figure 9), it is a set of iso-brightness contours that connects the surface gradients which appear the same brightness.

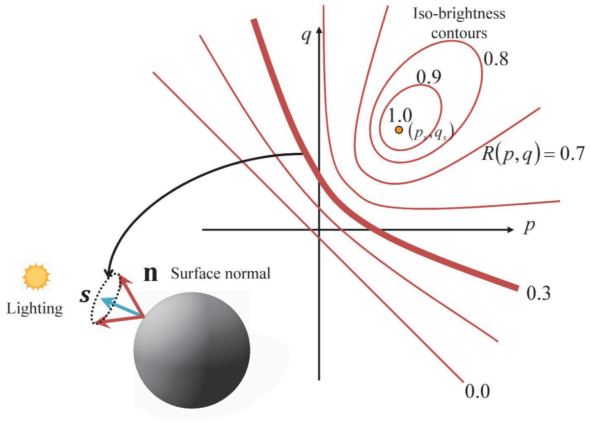

Figure 9. Reflectance map

In order to solve the SfS problem, it is necessary to calculate the surface gradients p and q using the known image brightness, then obtain the depth of the surface through the relationship between surface gradients and depth. However, since only one image brightness value is known, it is impossible to calculate two unknowns p and q. In order to solve this problem, it is necessary to regularize the problem by introducing attributes and assumptions about the surface shape of the target object. Regarding the methods of regularization, the solutions of SfS can be classified into four categories [8]: minimization approaches, propagation approaches, local approaches, and linear approaches.

2.2 Four approaches for SfS problem

2.2.1 Minimization approaches

Minimization approaches solve the SfS problem by minimizing the energy function which is composed of various constraints over the entire image. The key of this approach is to introduce appropriate constraints to construct energy equation. The commonly used constraints include the following four constraints.

Brightness constraint indicates the total brightness error of the reconstructed image compared with the input image, and is given by

$$\iint \big(I(x,y) - R(p,q)\big)^2 dxdy \tag{2.6}$$

Smoothness constraint ensures a smooth surface in order to stabilize the convergence to a unique solution, and is given by

$$\iint \big(p_x^2 + p_y^2 + q_x^2 + q_y^2\big)^2 dxdy \tag{2.7}$$

Intensity gradient constraint requires that the intensity gradient of the reconstructed image be close to the intensity gradient of the input image in both the x and y directions, and is given by

$$\iint ((R_x - I_x)^2 + \big(\big(R_y - I_y\big)^2\big) dxdy \tag{2.8}$$

Integrability constraint ensures valid surfaces, that is, $z_{x,y} = z_{y,x}$, and is given by

$$\iint ((z_x - p)^2 + \big(\big(z_y - q\big)^2\big) dxdy \tag{2.9}$$

There are many minimization approaches proposed by researches, here introducing several approaches that are commonly used.

One of the earliest minimization approaches is proposed by Ikeuchi and Horn [9]. They constructed their energy function using brightness constraint and smoothness constraint, then calculated shape by minimizing the energy function iteratively, using occluding boundary information to supply boundary conditions. In order to incorporate occluding boundary information, they proposed a method that employ stereographic plane to express the orientation of surface patches, rather than more commonly used gradient space.

Lee and Kuo [10] used brightness constraint and smoothing constraint, and proposed a method that combine SfS with triangular element surface model. This method approximates surface by the union of triangular patches, directly relates the image brightness to nodal height. By using brightness errors as cost function, the SfS problem becomes a quadratic function minimization problem with node height as parameter. Then the smoothness constraint is added to cost function to iteratively obtain the height of all nodes.

Horn [11] also proposed a method that uses brightness constraint and integrability constraint. This method enforces integrability of the surface gradient field, and it is able to reconstruct the surface height z and the surface gradients p and q simultaneously.

The energy function is shown as following,

$$\iint \big(I(x,y) - R(x,y)\big)^2 + \mu((z_x - p)^2 + \big(\big(z_y - q\big)^2\big) dxdy \tag{2.10}$$

where μ is a weighting factor.

Then minimizing this energy function. Since no partial derivatives of p and q appear in this equation, the minimization of this equation is an ordinary calculus problem. Differentiating equation (2.10) with respect to p and q and setting the resulting equation to zero, it leads to

$$\begin{aligned} p &= z_x + \frac{1}{\mu}(I - R)R_p \\ q &= z_y + \frac{1}{\mu}(I - R)R_q \end{aligned} \tag{2.11}$$

Since z does not appear in brightness constraint part, the problem reduces to minimize the integrability error part. The Euler equation for this variational problem is

$$\Delta z = p_x + q_y \tag{2.12}$$

Using the discrete approximation of the Laplacian operator $\{\Delta f\}_{ij} = \varepsilon^2/\kappa\,(\bar{f}_{ij} - f_{ij})$ leads to

$$z_{ij}^{(n+1)} = \bar{z}^{(n)} - \frac{\varepsilon^2}{\kappa}(p_x + q_y) \tag{2.13}$$

where $z_{i,j}^{(n+1)}$ is the z value of pixel (i,j) at iteration $n+1$, $\bar{z}$ is the local average of z at iteration n. κ is the number of nonzero entries in the discrete Laplacian filter minus one, κ = 4 when the local average z is computed using the four adjacent neighbors. ε is the spacing between image cells.

The coupled system of equations for p, q, z suggests an iterative scheme,

$$\begin{aligned} p_{ij}^{(n+1)} &= \{z_x\}_{ij}^{(n)} + \frac{1}{\mu}(I - R)R_p \\ q_{ij}^{(n+1)} &= \{z_y\}_{ij}^{(n)} + \frac{1}{\mu}(I - R)R_q \\ z_{ij}^{(n+1)} &= \bar{z}_{ij}^{(n)} - \frac{\varepsilon^2}{\kappa}(\{p_x\}_{ij}^{(n+1)} + \{q_y\}_{ij}^{(n+1)}) \end{aligned} \tag{2.14}$$

Zheng and Chellappa [12] introduced intensity gradient constraint and constructed their energy function using brightness constraint, intensity gradient constraint and integrability constraint. Their energy function is expressed as,

$$\iint F(p,q,z)dxdy$$

$$F = \big(I(x,y) - R(p,q)\big)^2 + ((R_x - I_x)^2 + (\big(R_y - I_y\big)^2) + \mu\left((p - z_x)^2 + \big(q - z_y\big)^2\right) \tag{2.15}$$

The minimization of equation (2.15) is equivalent to solving the following Euler equations,

$$\begin{aligned} F_p - \frac{\partial}{\partial x}F_{p_x} - \frac{\partial}{\partial y}F_{p_y} &= 0 \\ F_q - \frac{\partial}{\partial x}F_{q_x} - \frac{\partial}{\partial y}F_{q_y} &= 0 \\ F_z - \frac{\partial}{\partial x}F_{z_x} - \frac{\partial}{\partial y}F_{z_y} &= 0 \end{aligned} \tag{2.16}$$

By approximating the reflectance map by Taylor series expansion of up to first-order terms, it is able to obtain expressions for $F_p, F_{p_x}, F_{p_y}, F_q, F_{q_x}, F_{q_y}, F_z, F_{z_x}, F_{z_x}$ in equation (2.16).

Giving the expression of p, q, z before and after updating,

$$p' = p + \delta p, \quad q' = q + \delta q, \quad z' = z + \delta z \tag{2.17}$$

where variable with prime ($'$) represent values after updating and variable without prime represent values before updating.

The corresponding increments in the derivatives of p, q, z after updating are

$$\begin{array}{ccc} {p_x}' = p_x - \delta p & {q_x}' = q_x - \delta q & {z_x}' = z_x - \delta z \\ {p_y}' = p_y - \delta p & {q_y}' = q_y - \delta q & {z_y}' = z_y - \delta z \\ {p_{xx}}' = p_{xx} - 2\delta p & {q_{xx}}' = q_{xx} - 2\delta q & {z_{xx}}' = z_{xx} - 2\delta z \\ {p_{yy}}' = p_{yy} - 2\delta p & {q_{yy}}' = q_{yy} - 2\delta q & {z_{yy}}' = z_{yy} - 2\delta z \end{array} \tag{2.18}$$

Then it is able to obtain expressions of F_p, F_{p_x}, F_{p_y} represented by $\delta p, \delta q, \delta z$.

$$\begin{aligned} 1/2\, F_p &= \big(R + R_p\delta p + R_q\delta q - I\big)R_p + \mu(p - z_x + \delta p + \delta z) \\ 1/2\, \frac{\partial}{\partial x}F_{p_x} &= \big(R_p p_{xx} + R_q q_{xx} - I_{xx}\big)R_q - 2R_p^2\delta p - 2R_pR_q\delta q \\ 1/2\, \frac{\partial}{\partial y}F_{p_y} &= \big(R_p p_{yy} + R_q q_{yy} - I_{yy}\big)R_q - 2R_p^2\delta p - 2R_pR_q\delta q \end{aligned} \tag{2.19}$$

The other terms in equation (2.16) can be derived similarly, and lead to the iterative scheme.

$$\begin{aligned} \delta p &= \tfrac{4}{\Delta}\Big(\big(C_1 - \tfrac{1}{4}\mu C_3\big)\big(5R_p^2 + \tfrac{5}{4}\mu\big) - \big(C_2 - \tfrac{1}{4}\mu C_3\big)\big(5R_pR_q + \tfrac{1}{4}\mu\big)\Big) \\ \delta q &= \tfrac{4}{\Delta}\Big(\big(C_2 - \tfrac{1}{4}\mu C_3\big)\big(5R_p^2 + \tfrac{5}{4}\mu\big) - \big(C_1 - \tfrac{1}{4}\mu C_3\big)\big(5R_pR_q + \tfrac{1}{4}\mu\big)\Big) \\ \delta z &= \tfrac{1}{4}(C_3 + \delta p + \delta q) \end{aligned} \tag{2.20}$$

where

$$\begin{aligned} C_1 &= \big(-R + E + R_p p_{xx} + R_q q_{xx} - E_{xx} + R_p p_{yy} + R_q q_{yy} - E_{yy}\big)R_p - \mu(p - z_x) \\ C_2 &= \big(-R + E + R_p p_{xx} + R_q q_{xx} - E_{xx} + R_p p_{yy} + R_q q_{yy} - E_{yy}\big)R_q - \mu\big(q - z_y\big) \\ C_3 &= -p_x + z_{xx} - q_y + E_{yy} \\ \Delta &= 4\left(\left(5R_p^2 + \frac{5}{4}\mu\right)\left(5R_q^2 + \frac{5}{4}\mu\right) - \left(5R_pR_q + \frac{1}{4}\mu\right)^2\right) \end{aligned} \tag{2.21}$$

This method uses a pyramid algorithm to do the calculation. It starts with the lowest resolution layer. The iterative scheme is used to update depth and gradients simultaneously at each layer. Then the result is up-sampled and used as the initial value for next layer until the final result is obtained.

2.2.2 Propagation approaches

Propagation approaches propagate shape information from certain surface points where the shape either is known or can be uniquely determined (such as singular points) to the entire image. The commonly used methods include characteristic strips method and minimum downhill method.

Horn proposed the concept of characteristic strip [13], that is, the curve traced out by solving the differential equations that composed of a first-order non-linear partial differential equation in two unknowns relating the intensity value to the shape of the object. The direction of characteristic strips is toward the intensity gradient. If the value at the starting point of this line is known, it is able to calculate the depth and orientation of the surface along this characteristic strip. The shape information is propagated outward along characteristic strips.

Bichsel and Pentland [14] proposed a minimum downhill method based on Oliensis's observation that the surface shape can be reconstructed from singular points instead of the occluding boundary. The minimum downhill principle used in their method is of the form: (1) Passing surface information only to pixels which are more distant to the light source (downhill principle). (2) Among different possible paths, choosing the path that leads the least away from the light source (minimum downhill principle).

For a surface point (x, y, z), taking a small step (dx, dy) and expressing it in polar coordinate ($dx = \cos\varphi\, ds, dy = \sin\varphi\, ds$). Setting surface normal for this point as $n(n_1, n_2, n_3)$, then they should satisfy the following equation:

$$dx \cdot n_1 + dy \cdot n_2 + dz \cdot n_3 = 0 \tag{2.22}$$

Letting the slope for surface be $k(\varphi, n) = \frac{dz}{ds}(\varphi, n)$. Then it is able to obtain,

$$k(\varphi, n) = -\frac{\cos\varphi n_1 + \sin\varphi n_2}{n_3} \tag{2.23}$$

For each direction $(\cos\varphi, \sin\varphi)$, finding the slope $k(\varphi)$ corresponding to the steepest ascent in this direction through the curve of constant brightness line of image-

irradiance equation.

$$\frac{d}{d\alpha}\cos\varphi\, p(\alpha) + \sin\varphi\, q(\alpha) = 0 \tag{2.24}$$

where α is an arbitrary parameter along the curve of constant brightness.

For each direction, there are two sets of solution. Then choosing the surface gradients that lead away from the light source according to the downhill principle.

$$(\cos\varphi\,, \sin\varphi, k(\varphi)) \cdot \vec{l} \geq 0 \tag{2.25}$$

The height of current point (x, y) is propagated from the height value of the neighboring point $(x + \cos\varphi\, ds, y + \sin\varphi\, ds)$. Usually it leads to different estimate height for each direction $(\cos\varphi\,, \sin\varphi)$,

$$\hat{z}^{t+1}(x, y, \varphi) = z^t(x + \cos\varphi\, ds, y + \sin\varphi\, ds) - k(\varphi)ds \tag{2.26}$$

where t is the number of iterations.

Among all possible directions, choosing the estimate $\hat{z}$ which brings $z(x, y)$ closest to the light direction.

$$\hat{z}^{t+1}(x, y) = \max\left(sup_{\varphi}\left(\hat{z}^{t+1}(x, y, \varphi)\right), z^t(x, y)\right) \tag{2.27}$$

According to the above calculation process, this method starts from the singular points, follows the principle of minimum downhill to propagate height information from current pixel to their neighboring pixels.

2.2.3 Local approaches

The local approaches derive the shape by assuming a local surface type. This type of approaches always assumes a local spherical shape feature and uses the intensity and its first and second derivatives to estimate shape information.

Pentland [15] suggests assumption that local surface is approximately spherical. It recovers shape information using the intensity value and its second derivatives. This method has no requirement for prior knowledge. The equations for tilt τ and slant σ are given as following,

$$\begin{aligned} \tan\tau &= \frac{-(I_{xx} - I_{yy}) \pm \sqrt{(I_{xx} - I_{yy})^2 + 4I_{xy}^2}}{2I_{xy}} \\ \cos\sigma &= \sqrt{\frac{(I_{xx} + I_{yy})\tan\tau - \sec^2\tau I_{xy}}{(I_{xx} + I_{yy})\tan\tau + \sec^2\tau I_{xy}}} \end{aligned} \tag{2.28}$$

There are two solutions for tilt in equation (2.28), one of them can be discarded because it results in an illuminant direction that behind the observed object. After

obtaining tilt and slant for each pixel, the surface gradients can be calculated according to equations (2.3) and (2.4).

Lee and Rosenfeld [16] follows the same local spherical assumption used in Pentland's method. To avoid high-order derivatives, they proposed a new method that only uses first derivatives of intensity to derive shape information through the addition of illumination coordinate system.

Normally the surface shape is defined in the viewer coordinate system (z-axis is the viewing direction). However, lee and Rosenfeld found out that it easier to calculate slant and tilt in the illumination coordinate system (z-axis is the illumination direction). They proposed a method that calculates tilt and slant in the illumination coordinate first, then transform back to the viewer coordinate.

They first give the transformation formula between illumination coordinate and viewer coordinate system.

$$(x', y', z')^T = \begin{pmatrix} \cos\tau_s \cos\sigma_s & \sin\tau_s \cos\sigma_s & -\sin\sigma_s \\ -\sin\tau_s & \cos\tau_s & 0 \\ \cos\tau_s \sin\sigma_s & \sin\tau_s \sin\sigma_s & \cos\sigma_s \end{pmatrix} (x, y, z)^T \quad (2.29)$$

where σ_s and τ_s are the slant and tilt of light source. (x, y, z) represents coordinates in viewer coordinate system, (x', y', z') represents coordinates in illumination coordinate system.

The tilt in illumination coordinate system can be obtained by

$$\tau = \arctan \frac{I_y \cos\tau_s - I_x \sin\tau_s}{I_x \cos\tau_s \cos\sigma_s + I_y \sin\tau_s \cos\sigma_s} \quad (2.30)$$

In illumination coordinate, the slant is the angle between the surface normal and illumination direction (z-axis), there is $\sigma = \arccos(\vec{N} \cdot \vec{L})$. If the reflectance map is given by $I = \lambda\rho\vec{N} \cdot \vec{L}$ (Lambert model), where λ and ρ are scalars representing the illumination intensity and reflectivity coefficient, then there is $\sigma = \arccos(I/\lambda\rho)$. Slant can be calculated by the ratio of intensity and $\lambda\rho$. $\lambda\rho$ at a certain point (P) can be estimated by the intensity values of two neighboring points (Q, R) of point P in the gradient direction at P and on opposite side of P.

After obtaining the slant and tilt in illumination coordinate system, using coordinate transform (equation (2.29)) to get surface slant and tilt in the viewer coordinate system.

2.2.4 Linear approaches

Linear approaches calculate the solution based on the linearization of the reflection function. The basic idea of this method is that in the reflection function, the low-order terms occupy the main part and the high-order terms can be ignored. There are two commonly used methods, one is proposed by Pentland, the other is proposed by Tsai and Shah.

Pentland [17] uses linear approximation of reflectance function, and applies Fourier transform to the linear function to obtain closed-form solutions for surface shape. They linearized the reflection function (equation (2.5)) by taking Taylor expansion of R around $(p, q) = (p_0, q_0)$ up through the first order terms.

$$I(x,y) = R(p_0,q_0) + (p-p_0)\frac{\partial R(p,q)}{\partial p}\Big|_{p=p_0,q=q_0} + (q-q_0)\frac{\partial R(p,q)}{\partial q}\Big|_{p=p_0,q=q_0} \quad (2.31)$$

For lambert reflectance function and $(p_0, q_0) = (0,0)$, equation (2.31) becomes,

$$I(x,y) = \cos\sigma + p\cos\tau\sin\sigma + q\cos\sigma\sin\tau \quad (2.32)$$

Then Pentland performed the Fourier transform on both sides of the above equation. Using the identities:

$$\begin{aligned} \frac{\partial}{\partial x}z(x,y) &= F_z(w_1,w_2)(-iw_1) \\ \frac{\partial}{\partial y}z(x,y) &= F_z(w_1,w_2)(-iw_2) \end{aligned} \quad (2.33)$$

where F_z is the Fourier transform of $z(x,y)$, then it is able to get,

$$F_I = F_z(w_1,w_2)(-iw_1)\cos\tau\sin\sigma + F_z(w_1,w_2)(-iw_2)\sin\tau\sin\sigma \quad (2.34)$$

where F_I is the Fourier transform of image $I(x,y)$.

The height result can be obtained by re-arranging the terms in the above equation and performing an inverse Fourier transform.

Tsai and Shah [18] proposed a method that applies the discrete approximation for gradients, then employs the linear approximation of the reflectance function in terms of the depth directly. Their algorithm recovers the depth at each point using iterative scheme. They first use the following discrete approximations for p and q.

$$p = \frac{\partial z}{\partial x} = z_{i,j} - z_{i,j-1},\ q = \frac{\partial z}{\partial y} = z_{i,j} - z_{i-1,j} \quad (2.35)$$

Then the reflectance function can be rewritten as:

$$f(z_{i,j}) = I_{i,j} - R(z_{i,j} - z_{i,j-1}, z_{i,j} - z_{i-1,j}) = 0 \quad (2.36)$$

Taking the Taylor expansion of above equation about $z_{i,j} = z_{i,j}^{n-1}$ up through the first order terms to obtain:

$$0 = f(z_{i,j}) \approx f(z_{i,j}^{n-1}) + (z_{i,j} - z_{i,j}^{n-1}) \frac{\partial f}{\partial z_{i,j}}(z_{i,j}^{n-1}) \tag{2.37}$$

For $z_{i,j} = z_{i,j}^{n}$ (the depth at n-th iteration), there is,

$$z_{i,j}^{n} = z_{i,j}^{n-1} + \frac{-f(z_{i,j}^{n-1})}{\frac{\partial f}{\partial z_{i,j}}(z_{i,j}^{n-1})} \tag{2.38}$$

where

$$\frac{\partial f}{\partial z_{i,j}}(z_{i,j}^{n-1}) = -1 * \left(\frac{(p_s+q_s)}{\sqrt{p^2+q^2+1}*\sqrt{p_s^2+q_s^2+1}} - \frac{(p+q)*(p*p_s+q*q_s+1)}{\sqrt{(p^2+q^2+1)^3}*\sqrt{p_s^2+q_s^2+1}}\right) \tag{2.39}$$

Assuming the initial value for z is 0 for all pixels, the depth result can be obtained using above equation iteratively. In most cases, one or two iterations is enough.

2.3 Advantages and disadvantages for these four approaches

Section 2.2 introduced four different categories of SfS approaches, including their principles, commonly used methods, and calculation formulas. This section analyzes the advantages and disadvantages of these approaches.

Minimization approaches solve the SfS problem by minimizing the energy function which is composed of various constraints. Commonly used constraints include the brightness constraint, the smoothness constraint, the integrability constraint, and the gradient constraint. This type of approaches considers various possible constraints in the imaging process, and when appropriate constraints are combined together, a more stable and accurate solution can be generated. However, when the algorithm searches for the minimum value, if the initial condition is unknown, it is easy to fall into the local minimum. And if the occlusion boundary condition is used as the initial value, the solution may have the concave/convex ambiguity. If the singularity (the maximum value of the image brightness value) is used as the initial condition, although the concave/convex ambiguity can be avoided, the singularity may be easily confused with the noise point, and may result in a large difference between the restored result and the expectation. Moreover, the general function variation and relaxation iteration commonly used in the minimum approaches will lead to a slow convergence problem.

Propagation approaches propagate shape information from certain surface points whose shape is known or can be uniquely determined to the entire image. Most commonly used one is the minimum downhill approach. The solution process of this method takes advantage of the relevant differentiable properties, which implicitly using the smooth surface assumption. Since this method incorporates the smoothness assumption into the algorithm rather than directly using it as a separate constraint function, the problem of over-smoothing due to the introduction of second-order differentiation can be avoided. Usually it is able to find the global optimal solution. However, this method is too complicated, and the amount of calculation will increase as the image size increases. And since this method is to transfer the shape information from several known points to the whole image, it requires strict prior knowledge (e.g. depth value of singularities). For actual images, this prior knowledge is very difficult to obtain. One way to do this is to assign the initial depth value for singular points as a fixed positive value and initialize the depth values for other points to large negative values as they did in reference 14. This usually works for synthetic images. But for actual images which include noises, it may occur large errors and resulting in unstable evolution.

Local approaches derive the shape by assuming a local surface type. This method mainly assumes a local spherical shape feature and uses the first and second derivatives of the intensities to calculate slant and tilt. This type of approaches is to solve the height value of the object surface by combining the reflection model with the assumed local shape of the surface to form equations about the local shape. Therefore, when the surface of the object satisfies the local shape assumption, this method works well, but it fails when the object surface does not satisfy shape assumptions. However, the local approach is simple and intuitive, it can directly obtain the local shape of the object surface without multiple iterations, the calculation is very fast.

Linear approaches calculate the solution based on the linearization of the reflection function. The basic idea of this method is that in the reflection function, the low-order terms occupy the main part and the high-order terms can be ignored. The linearized result after performing the Taylor expansion and discarding the nonlinear term is very close to the original function. Therefore, this method works well for surface whose higher order terms are not significant, but it fails when higher order terms are more

important. And similar to the local method, since it uses the linearization assumption of the reflection function, the recovery result is only an approximation to the real solution. Again, its calculation is very fast.

3 Experimental results for SfS

3.1 Experimental results for selected SfS algorithms

3.1.1 Four selected SfS algorithms

According to the analysis in section 2.3, these four types of approaches use different assumptions about the surface shape, and each has their own advantages and disadvantages. It may be not objective and accurate enough to determine which type of approach is more suitable for processing the image on planetary surface only by theoretical analysis, therefore all four approaches are tested here.

In this section, we implemented one minimization, one propagation, one local, and one linear method. An important criterion for method selection is whether the method is easy to find and easy to make an implementation.

For minimization approaches, four algorithms are mainly introduced in section 2.2.1. Lee and Kuo's method approximates surface by a union of triangular patches. According to the experimental results in reference 2, the calculation time for a synthetic image with 128 x 128 pixels is over 100s. It is significantly slower than other approaches, thus this method is not considered. The other three methods use variational calculus to minimize the energy function. Among them, Zheng and Chellappa's method uses intensity gradient constraint instead of smoothness constraint (which may cause over-smoothing problem) to ensure the convergence of iteration process. It also incorporates integrability constraint, thus it is able to reconstruct the surface height z and surface gradients p and q simultaneously. And there is no special requirement for the initialization of the boundary, the initial values for both depth and gradients can be zero. Therefore, Zheng and Chellappa's method is chosen.

For propagation approaches, characteristic strips method and minimum downhill method are introduced in section 2.2.2. Characteristic strips method propagates shape information along the characteristic strips, and the initial known curve is required. This initial surface curves are often constructed around the neighborhoods of singular

points using a local spherical shape assumption and several additional information, the local normal of singular points and whether the surface is convex or concave with respect to the observer at this point. Compared with this method, minimum downhill method requires less additional information that only the depth value of singular points is needed. It is simpler and easier to implement, and it can directly recover depth and guarantee a continuous surface. Therefore, the minimum downhill method is chosen.

For local approaches, Pentland's method, Lee and Rosenfeld's method are introduced in section 2.2.3. These two methods follow the same local spherical assumption. Pentland's method recovers the shape using the first and second-order derivatives of intensity. Lee and Rosenfeld's method is an improved method based on Pentland's method. They proposed coordinate transformation between viewer coordinate system and illumination coordinate system, which simplify the calculation. And their method only uses first derivatives of intensity to derive shape information, which is able to avoid problem caused by high-order derivatives and less sensitive to noises. Therefore, Lee and Rosenfeld's method is chosen.

For linear approaches, Pentland's method, Tsai and Shah's method are introduced in section 2.2.4. Pentland's method uses the linear approximation of the reflectance function in terms of surface gradients and applies Fourier transform to the linear function to obtain depth at each point. Tsai and Shah's method applies the discrete approximation of surface gradients first, then employs the linear approximation of the reflectance function in terms of the depth directly. Since Pentland's method uses Fourier transform and inverse Fourier transform, it is time consuming. While Tsai and Shah's method does not, it is simpler and faster. Therefore, Tsai and Shah's method is chosen.

3.1.2 Experimental results

Here, we used the observation data of KAGUYA (SELENE) disclosed by reference 19. This archive provides the images of lunar surface and the corresponding digital elevation maps (DEMs). The main purpose of this section is to compare the results of four selected methods and to determine which method is most suitable for this research. Therefore, here using a relatively simple mosaic image to perform

experiments. This mosaic image is created from multiple lunar surface images with less shadow parts, thus it is a relative clean image with less noises.

Since the image used here is a mosaic image that composed of several images taken in real-time, the direction of the light source is not given. Here we used the method proposed in reference 16 to estimate the light source direction. In reference 16, they used the assumption that the changes in surface orientation are isotropically distributed. When this assumption is translated into a mathematical statement in terms of tilt and slant, the probability density function for slant is $(\sin\sigma)/2\pi$. Then they proved that the tilt and slant of illumination direction can be estimated by expectations of image and expectations of the first derivatives of image, which are

$$\begin{aligned} \tau_L &= \arctan(E\{I_y\}/E\{I_x\}) \\ \sigma_L &= \arccos(\frac{3E\{I^2\}}{\lambda^2\rho^2} - 1) \end{aligned} \tag{3.1}$$

where τ_L, σ_L are the tilt and slant of illumination direction, the expectation is taken over the given image region.

The size of image we used here is 512 x 512 pixels. The image and corresponding DEM are shown in Figure 10 (a), (b), respectively. Four selected SfS methods, Zheng and Chellappa's method, Bichsel and Pentland's method, Lee and Rosenfeld's method, Tsai and Shah's method were applied to the image. In the implementation of Zheng and Chellappa's method, the weighting factor for integrability constraint μ is set to 1 as suggested by authors. In the implementation of Bichsel and Pentland's method, the initial depth values for singular points are all assigned to a fixed positive value. The height detection results are shown in Figure 11. Since the calculation result of SfS is relative height value, the height range of the detection results are mapped to the same height range as the DEM.

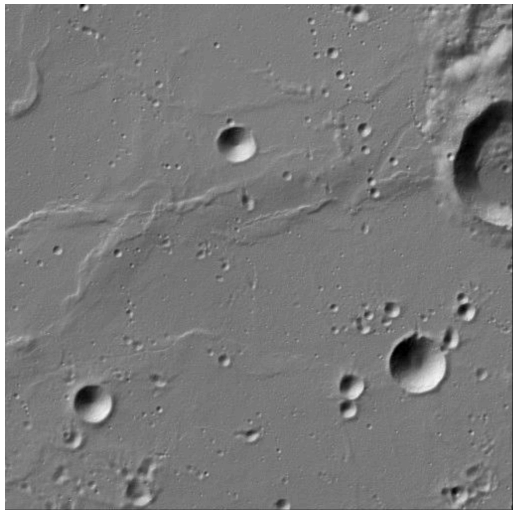

(a) Image

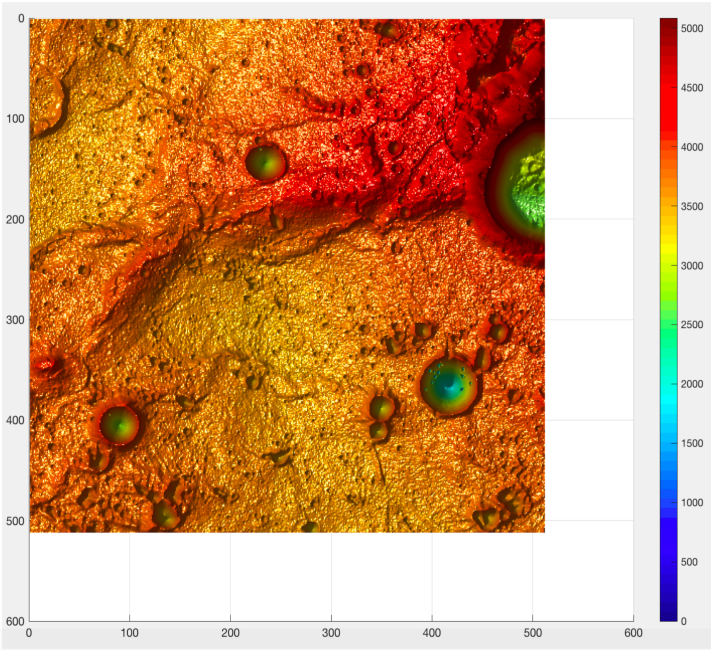

(b) DEM

Figure 10. Image and corresponding DEM for lunar surface

According to the detection results in Figure 11, it can be seen that the detection result of Bichsel and Pentaland's method is very bad, it cannot restore the surface shape at all. This is due to the inaccuracy of the given initial information, that is, the depth value of singular points. This method requires prior knowledge, the depth value for certain surface points need to be known. Since this prior knowledge is not available, we directly assigned the depth of singular points to a same positive value.

Then the shape information of these singular points is propagated to the surrounding points, in this process, the error of them is also propagated. If the prior knowledge is not accurate enough, it will directly lead to poor recovery result. For synthetic image which is simpler and with fewer noises, using depth value of singular points as prior knowledge may work well. But for real image, the singular points and noises are often mixed together, thus the noise point may be mistakenly selected as a singular point. Also, since the actual depth value of each singular points is different, assigning them as same value is not reasonable. Therefore, this method is not suitable for real planetary surface images.

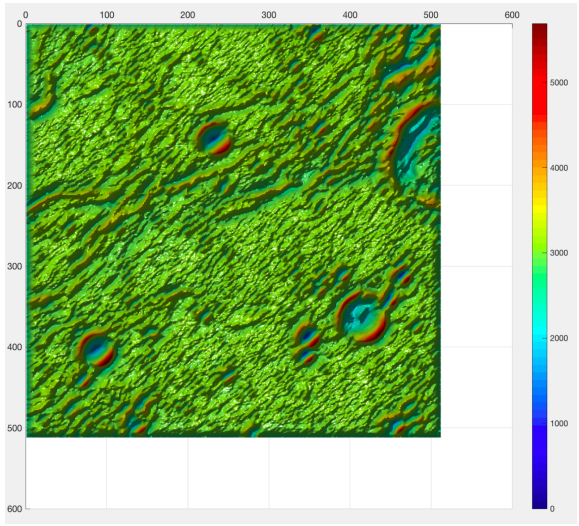

(a) Zheng and Chellappa's method

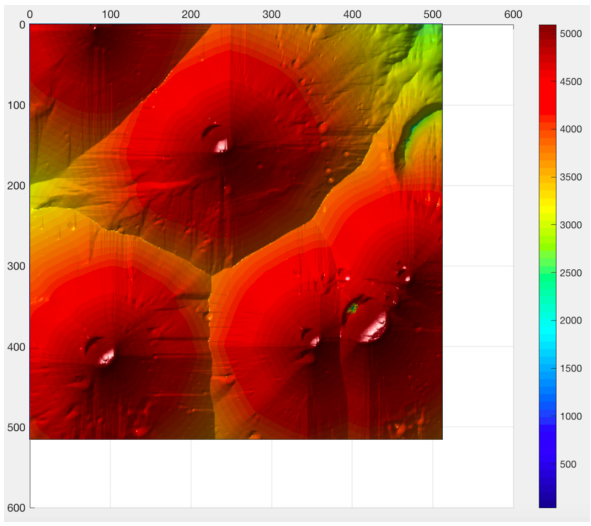

(b) Bichsel and Pentland's method

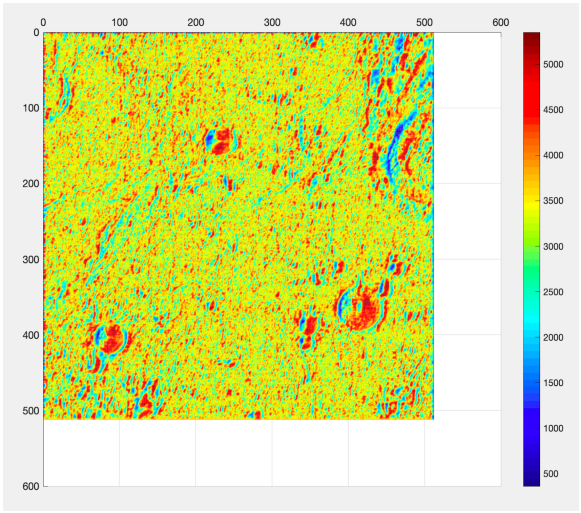

(c) Lee and Rosenfeld's method

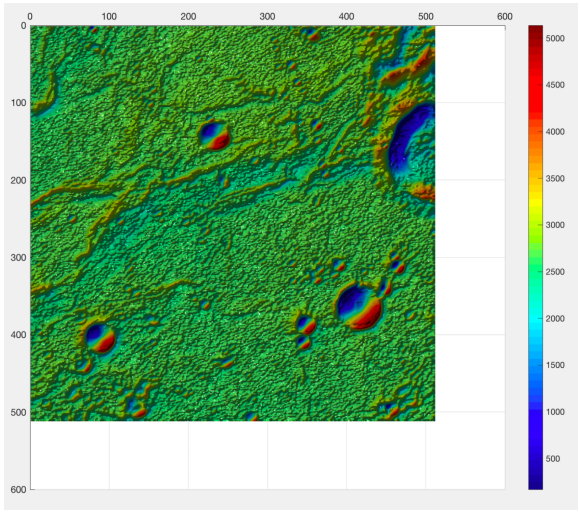

(d) Tsai and Shah's method

Figure 11. Height detection results for four SfS methods

The detection result of Lee and Rosenfeld's method is also poor. Although the position of the craters can be roughly detected, the overall result is very bad, there are lots of noise points and it is difficult to see the overall terrain changes. This is because that this method estimates depth using local spherical assumption and intensity derivatives. It is very sensitive to noises and not suitable for non-spherical surfaces.

This is because that when there is no available prior knowledge, this method tends to fall into a local minimum when searching for the minimum value (if the height values of singular points are used as prior knowledge, the same problem as in Bichsel and Pentlang's method will occur). Also, there are distortions along image discontinuities. While for Tsai and Shah's method, it shows the best result. The approximate shape is recovered, and it is able to preserve more details.

There are mainly two problems with these two methods: (1) The reconstruction results of craters are not good. The image of crater has the feature that the part facing the direction of the light source is very bright, and the rest part facing away from the light source is very dark. SfS estimates shape information based on the intensity value of each pixel, it cannot process shadow parts, thus the shape of craters cannot be recovered well. In the detection result of Zheng and Chellapa's method, the height value of edges of craters tends to be too high. In the detection results of Tsai and Shah's method, the height result of craters presents a problem that the partial height value is too high, and the partial height value is too low. (2) The reconstruction result of regions that height slowly changing is not good. For this kind of feature, the intensity values change is also not obvious. It is very hard for SfS to capture these slow changes, thus the error of recovered height of this part is large.

Based on the above analysis, Bischel and Pentland's method, Lee and Rosenfeld's method are not applicable for this research. The height values recovered from Lee and Rosenfeld's method, Tsai and Shah's method are not accurate, but the positions where the height value changes can be detected. Since the error of height value is very large, it is not meaningful to compare the height results directly with the DEM. So here first using height detection results to calculate the slope results (the change in height value), then comparing the slope detection results with slope map calculated from DEM for quantitative analysis. The slope results are shown in Figure 12 (a), (b), the slope map calculated from DEM is shown in Figure 12 (c). Figure 13 shows slope

error results for Lee and Rosenfeld's method, Tsai and Shah's method, respectively. The mean error and standard deviation of slope error are shown in Table 1. From the slope results, it can be seen that the slope error of these two methods are not much different. Both methods can detect the large slope changes but failed to detect small changes and details. The main problem is the crater parts and areas that height gradually changing.

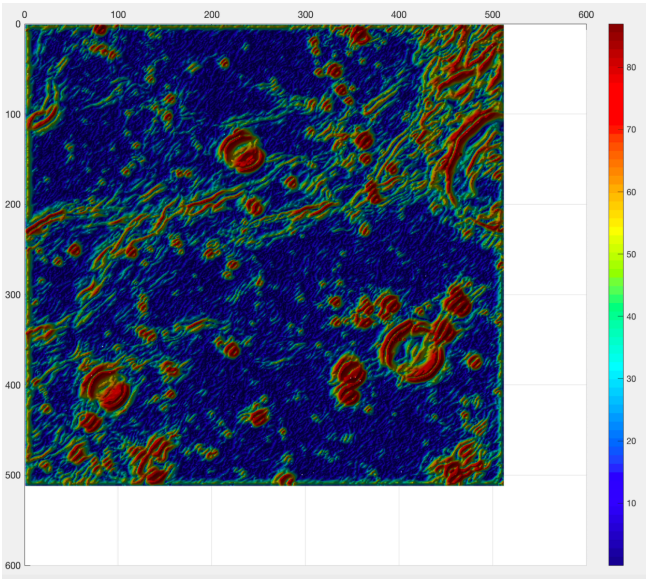

(a) Zheng and Chellappa's method

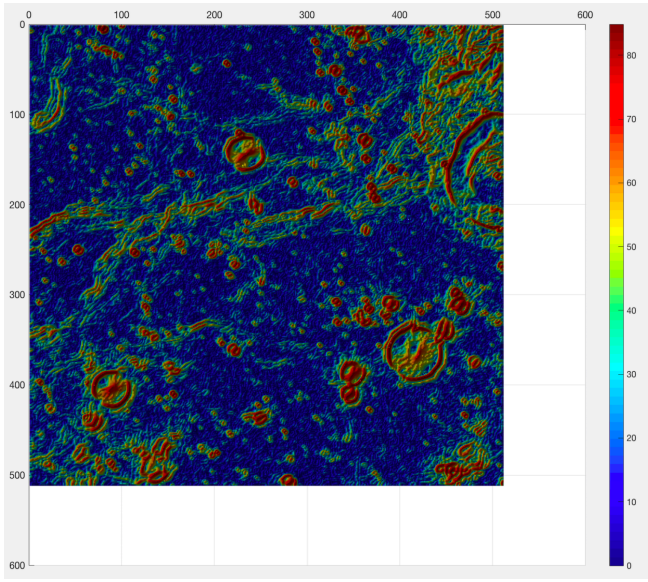

(b) Tsai and Shah's method

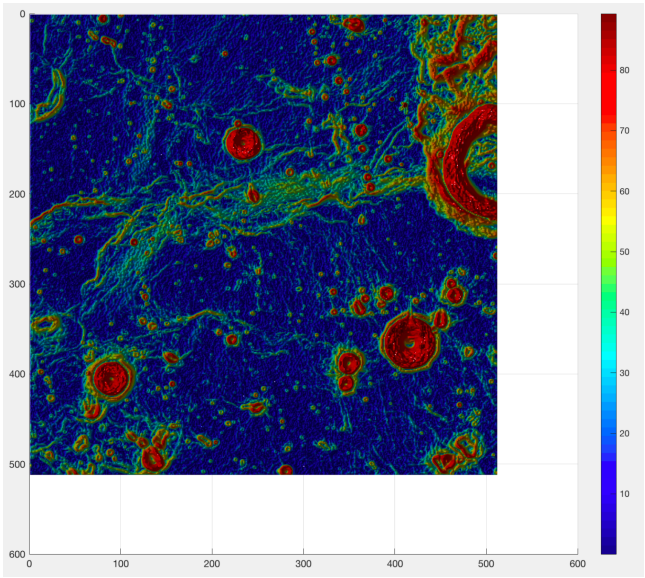

(c) Slope map generated from DEM

Figure 12. Slope detection results

3.1 Experimental results for selected SfS algorithms

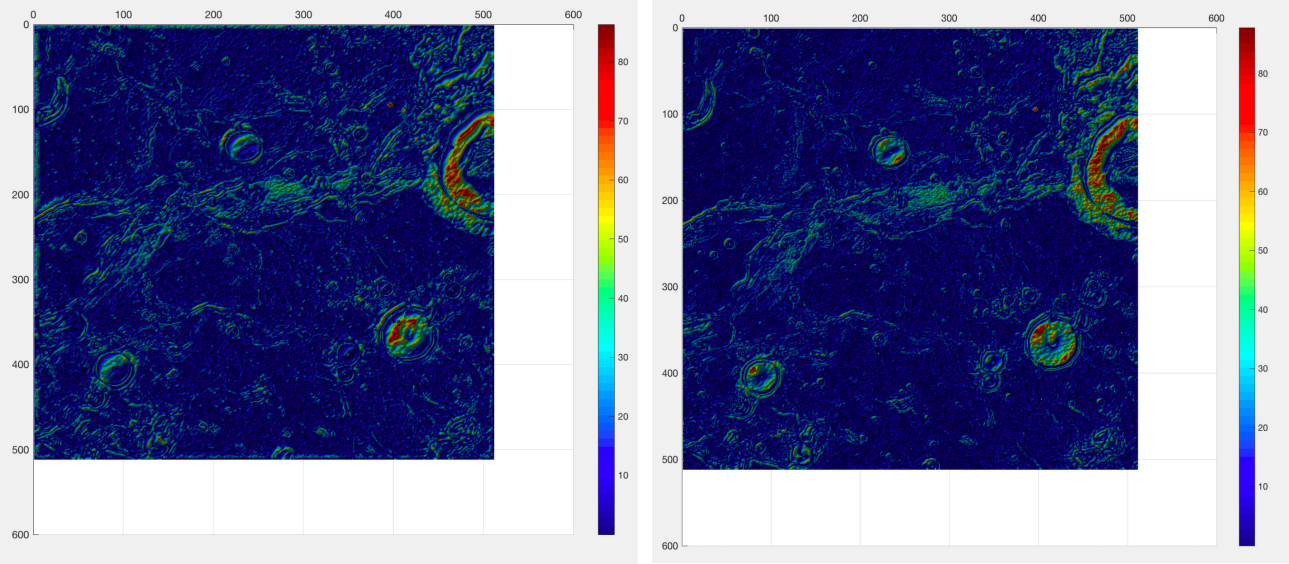

(a) Zheng and Chellappa's method (b) Tsai and Shah's method

Figure 13. Slope error results

Table 1. Average and standard deviation of slope error

Methods	Average slope error (°)	Standard deviation of slope error (°)
Zheng and Chellappa	12.8003	11.9930
Tsai and Shah	11.7996	11.9475

Table 2 gives the computation time for these four methods.

Table 2. Computation time for four methods

Methods	Computation time (s)
Zheng and Chellappa	12.012066
Bichsel and Pentland	5.270131
Lee and Rosenfeld	0.895480
Tsai and Shah	1.238389

Based on the experimental results (the height detection results in Figure 11 and the slope results in Figure 12, 13) and the theoretical analysis in section 2.3, it can be concluded that:

(1) Propagation approach is not suitable for this research. This approach requires prior knowledge (e.g. the height of singular point(s)), while it is difficult to obtain such priori knowledge in the actual image. We tried to deal with this problem by setting the height values of all singularities to the same value and used as prior knowledge as Bichsel and Pentland did. However, the detection result shows that it did not work well, the basic shape was failed to be recovered.

(2) Local approach is not suitable for this research. This approach often assumes a local spherical shape feature and uses derivatives of the intensities to recover shape information. It is simple and fast. But it only works well when the surface of the object satisfies the local shape assumption. It is not suitable for non-spherical surfaces and very sensitive to noise. The detection result is very noisy and failed to capture the overall terrain changes.

(3) Minimization approach can reconstruct the three-dimensional topography of the lunar surface. Since this method obtains solution of SfS by minimizing the energy function, the constraints used for constituting the energy function will directly affect the detection results. It is very important to choose the appropriate constraints. We tested the Zheng and Chellappa's method which considers three constraints, brightness constraint, intensity gradient constraint and integrability constraint. The detection result shows that this method is able to recover the approximate shape, but there are distortions along image discontinuities. And the calculation time is the longest.

(4) Linear approach shows best performance. This approach recovers shape based on the linearization of the reflection function. The algorithm is relatively simple, does not require priori knowledge about occlusion boundaries or singular points. The detection result shows that this method can recover the approximate shape, while preserving more details. And since the search for solutions is limited to a local range, the algorithm is quite fast.

Therefore, the Tsai and Shah’s method (linear approach) is chosen for this research.

3.2 Hapke model

In the previous section, the lambert model was used to implement experiments. This most commonly used model in the traditional solution of SfS is too simple. In order to further improve the detection results, we considered using another model which is more suitable for the reflection characteristics of the planetary surface, Hapke bidirectional reflection model.

3.2.1 Introduction of Hapke model

Hapke model, proposed by Bruce Hapke [21], is a bidirectional reflection model that considers multiple scattering (isotropic) and particle mutual shadowing effects. It is designed to study light scattering properties of planetary surfaces. It is based on radiation transmission, divides the received radiation into two parts: single-scattered radiation and multiple-scattered radiation. The single-scattered radiation is accurately calculated, and the multiple-scattered radiation is assumed to be isotropic. Figure 14 shows the geometry of the light source, target surface, and viewpoint in the Hapke model. The bidirectional reflectance function is expressed as equation (3.2).

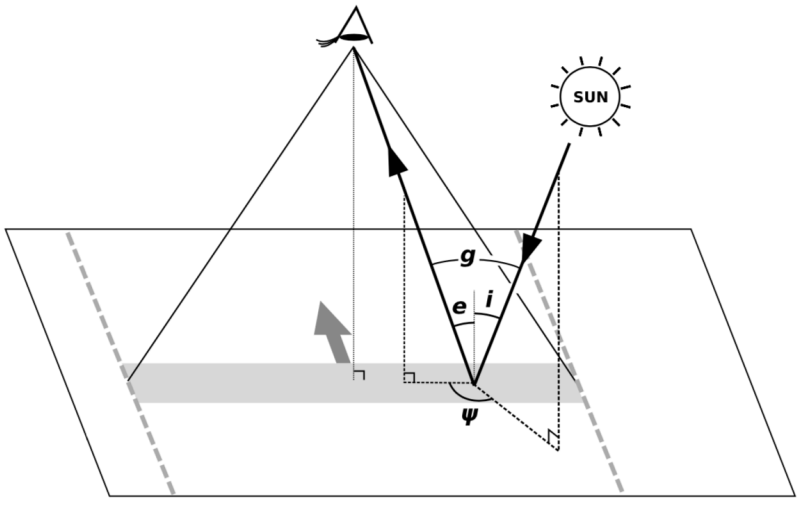

Figure 14. Schematic diagram of geometry of Hapke model

$$R(i,e,g)=\frac{w}{4\pi}\frac{\mu_0}{\mu_0+\mu}\left\{\left(1+B(g)\right)\cdot p(g)+H(\mu_0)H(\mu)\right\}S(i,e,g,\overline{\theta}) \quad (3.2)$$

where i is the incident angle, e is the emission angle, g is the phase angle, w is the particle single-scattering albedo, μ_0 and μ are $\cos i$ and $\cos e$, respectively.

The opposition effect functions B include the Shadow-Hiding Opposition Effect (SHOE) function $B_{SH}(g)$ and the Coherent Backscatter Opposition Effect (CBOE) function. They are expressed as:

$$B_{SH}(g)=\frac{B_{S0}}{1+(1/h_s)\tan(g/2)} \quad (3.3)$$

where h_s is the width of SHOE, B_{S0} is the amplitude of SHOE.

$$B_{CH}(g)=B_{C0}\frac{1+\frac{1-e^{-(1/h_C)\tan(g/2)]}}{(1/h_C)\tan(g/2)]}}{2[1+(1/h_C)\tan(g/2)]^2} \quad (3.4)$$

where h_C is the width of CBOE, B_{C0} is the amplitude of CBOE.

The single-particle angular scattering function $p(g)$ represents the change in the reflected light intensity with respect to the phase angle in the case of single scattering. Various phase functions have been proposed in which the empirical equation of the Henyey-Greenstein phase function is given by:

$$p(g)=\frac{1-\xi^2}{(1+2\xi\cos g+\xi^2)^{3/2}} \quad (3.5)$$

where ξ is asymmetry parameter.

H-functions are for isotropic scattering, which can be approximated by:

$$H(x)=\frac{1+2x}{1+2\,\gamma x} \quad (3.6)$$

where x is either μ_0 or μ, $\gamma=\sqrt{1-w}$.

The shadowing function S corrects the measured bidirectional reflectance for a smooth surface to the reflectance of the same surface characterized by a mean slope (photometric roughness) angle $\overline{\theta}$, which is a measure of the surface texture at a resolution that is below the detector limit.

The Hapke model contains lots of parameters, and the value of each parameter varies according to the terrain type. Reference 22 gives the values of Hapke parameters for several asteroids, as shown in table 3 (CBOE is not considered).

Table 3. Hapke parameters for several asteroids

Object	Phase	w	B_{S0}	h_s	ξ	θ
Ave. C-type	<25°	0.037±0.003	1.03±0.01	0.025±0.001	-0.47±0.01	(20°)
Ave. S-type	<25°	0.23±0.02	1.32±0.03	0.020±0.001	-0.35±0.01	(20°)
Geres (G)	1-22°	0.057±0.004	1.58±0.01	0.059±0.006	-0.40±0.01	(20°)
Vesta (V)	2-25°	0.040±0.03	1.03±0.10	0.044±0.010	-0.30±0.03	(20°)
Ida (S)	1-110°	$0.218^{+0.024}_{-0.010}$	1.53±0.10	0.020±0.005	-0.33±0.01	18±2°
Mathilde (C)	1-140°	0.035±0.006	3.18±1.0	0.074±0.003	-0.25±0.04	19±5°

3.2.2 Simplification of Hapke model

As mentioned in the previous section, Hapke model contains many free parameters, the values of these parameters are different for different topography. And the accurate determination of these free parameters directly from the data inversion (model fitting) is difficult. In order to minimize this issue and reduce the computation, the Hapke model is simplified according to reference 23.

Theoretically, the coherent backscatter opposition effect (CBOE) dominates only at very low phase angles (< 3◦), thus CBOE is not considered here. The calculation of shadowing function S is too complex and it is ignored here. Then further simplifying the model by setting $B_{CH}(g)$ to 0 and setting $p(g)$ to 1. According to the analysis in reference 23, the scattering of lunar surface can be considered isotropic, thus $p(g)$ is set to 1, then the phase angle is negligible, thus $B(g)$ is 0. This not only simplifies the expression of the Hapke model, but also guarantees that singularity does not occur, and retaining the basic properties of the Hapke model. The simplified model is expressed as:

$$R(i,e) = \frac{w}{4\pi}\frac{\cos i}{\cos i+\cos e}\frac{1+2\cos i}{1+2\gamma\cos i}\frac{1+2\cos e}{1+2\gamma\cos e} \tag{3.7}$$

Now there are only three parameters, incident angle i, emission angle e and single-scattering albedo w are needed. The parameter w is selected according to Hapke parameters of the moon table given in reference 24, w is set to 0.25 corresponding to average terrains. Angle i and e are related to the sun position and

camera position when the photo was taken and can be obtained from the image description file.

Then combining this simplified Hapke model with the Tsai and Shah's method. For light source direction $\vec{L} = (-p_s, -q_s, 1)$, and camera direction $\vec{C} = (-p_e, -q_e, 1)$, we can get:

$$\cos i = \frac{\vec{n}\cdot\vec{L}}{|n|\cdot|L|} = \frac{1+pp_s+qq_s}{\sqrt{1+p^2+q^2}\sqrt{1+p_s^2+q_s^2}} \tag{3.8}$$

and

$$\cos e = \frac{\vec{n}\cdot\vec{C}}{|n|\cdot|C|} = \frac{1+pp_e+qq_e}{\sqrt{1+p^2+q^2}\sqrt{1+p_e^2+q_e^2}} \tag{3.9}$$

Substituting the above two expressions into equation (3.7) gives the reflectance function of the Hapke model in terms of surface gradients (p, q):

$$R(p,q) = \frac{w}{4\pi}\frac{C_eF_s}{C_sF_e+C_eF_s}\frac{FC_s+2F_s}{FC_s+2\gamma F_s}\frac{FC_e+2F_e}{FC_e+2\gamma F_e} \tag{3.10}$$

where

$$C_s = \sqrt{1+p_s^2+q_s^2} \tag{3.11}$$

$$C_e = \sqrt{1+p_e^2+q_e^2} \tag{3.12}$$

$$F_s = 1+pp_s+qq_s \tag{3.13}$$

$$F_e = 1+pp_e+qq_e \tag{3.14}$$

$$F(p,q) = \sqrt{1+p^2+q^2} \tag{3.15}$$

Similar to the analysis process of Tsai and Shah's method described in section 2.2.4, using the finite difference to get a discrete approximation of surface gradients, then getting the iterative scheme as follows.

$$f\left(z_{i,j}\right) = I_{i,j} - R\left(z_{i,j} - z_{i,j-1}, z_{i,j} - z_{i-1,j}\right) = 0 \tag{3.16}$$

$$z_{i,j}^{n} = z_{i,j}^{n-1} - \frac{f\left(z_{i,j}^{n-1}\right)}{\frac{\partial f}{\partial z_{i,j}}\left(z_{i,j}^{n-1}\right)} \tag{3.17}$$

Assuming the initial estimate is $z_{i,j}^{0} = 0$ for all pixels, the depth can be iteratively derived using above equation.

3.3 Experimental results for SfS with Hapke model

In section 3.1.2, in order to facilitate the verification of which SfS method is more

suitable for this research, we used the mosaic image composed of multiple lunar surface images for experiments. From here, we perform experiments using images taken by the spacecraft in real time. Here we used the data from KAGUYA (SELENE) disclosed by reference 19, and data from Lunar Reconnaissance Orbiter Camera (LROC) disclosed by reference 20. The incident angle and emission angle are given by the image description file. Experiments were performed on three sets of data. The detection results are shown in Figure 15, 16 and 17 respectively. In order to compare the height detection result with the DEM, the height range of the detection result is mapped to the same height range as the DEM.

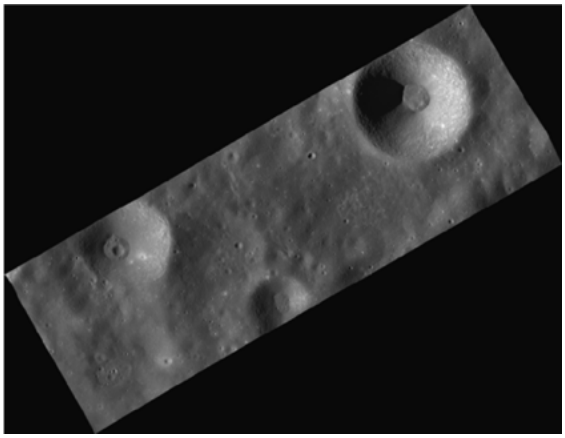

(a) Lunar surface image

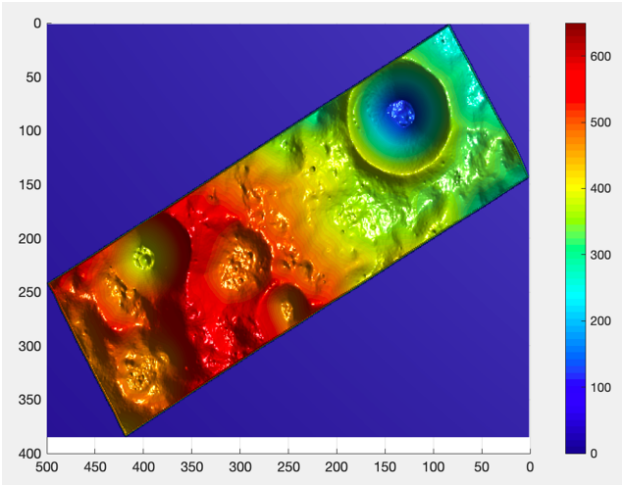

(b) Corresponding DEM

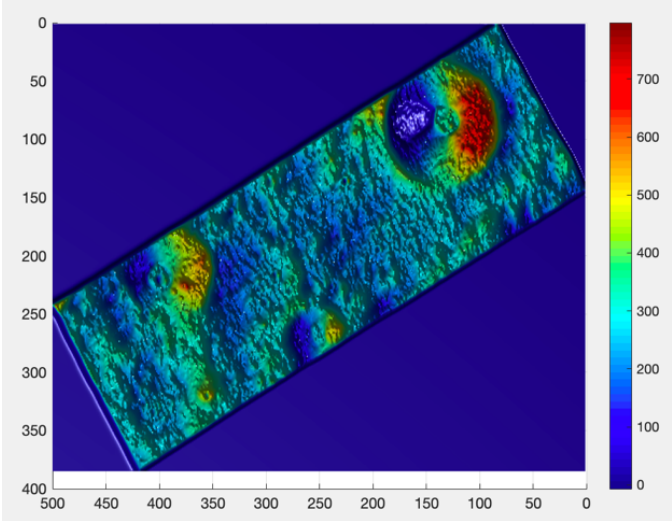

(c) Detection result

Figure 15. Lunar surface image, corresponding DEM and detection result for data 1

3.3 Experimental results for SfS with Hapke model

.

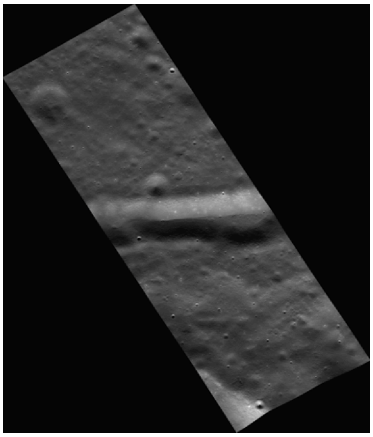

(a) Lunar surface image

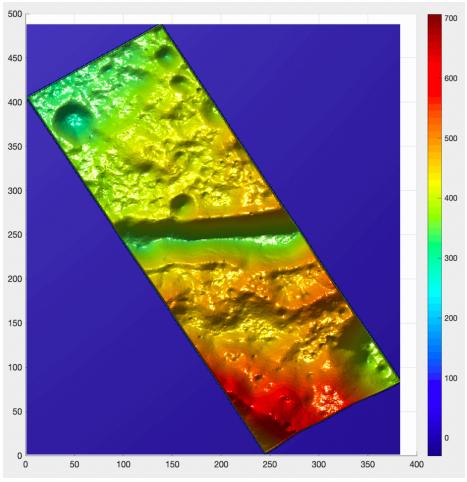

(b) Corresponding DEM

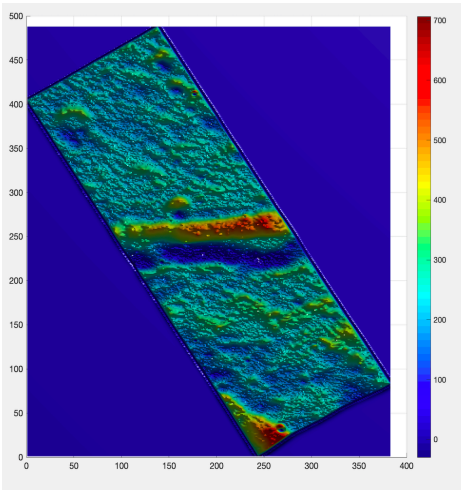

(c) Detection result

Figure 16. Lunar surface image, corresponding DEM and detection result for data 2

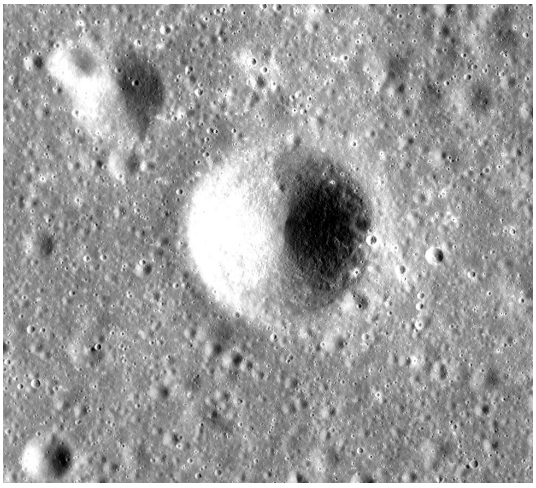

(a) Lunar surface image

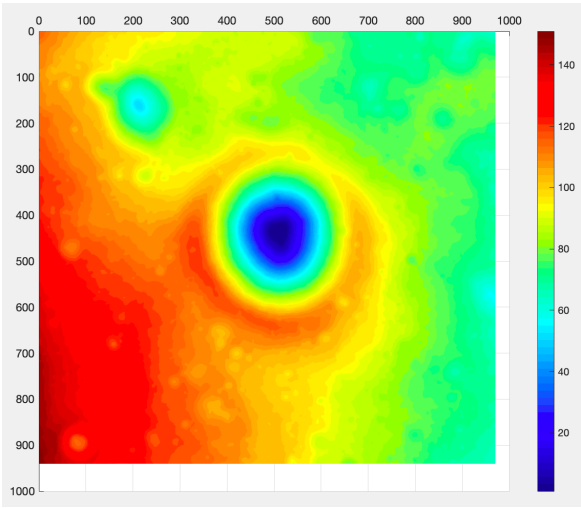

(b) Corresponding DEM

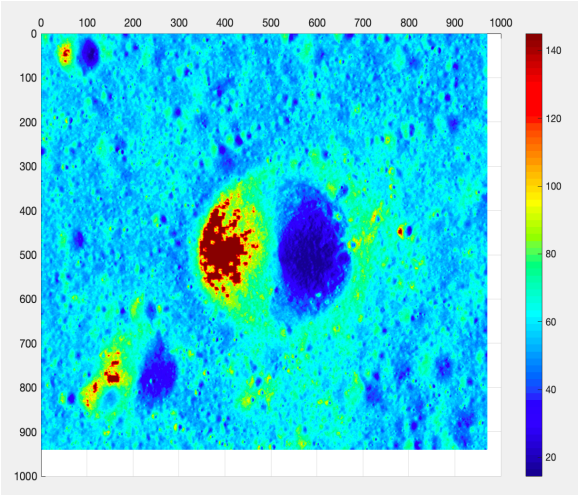

(c) Detection result

Figure 17. Lunar surface image, corresponding DEM and detection result for data 3

By observing the height detection results, it can be found that:

(1) Similar to the experimental results in section 3.1.2, even if the Hapke model which is more consistent with lunar surface reflection is used, SfS can only roughly recover the approximate shape, the error of height value is still large.

(2) Although the height value error is large, it is able to detect the position that height changes, that is, SfS is effective for detecting obvious obstacles.

(3) Unlike the mosaic image used in section 3.1.2, there are many shadow parts in the image captured in real time. Since SfS recover the object's three-dimensional shape according to the distribution of image brightness, it cannot process shadow. Therefore, the height values of these shadow parts cannot be correctly recovered.

(4) Different types of obstacles have different detection results. For obstacles that have obvious characteristics such as craters and valleys, they can be clearly detected. However, the slope surfaces cannot be detected, the overall terrain of detection result tends to be flat. Thus the detection results for different types of terrains are discussed separately.

The images, corresponding DEMs and detection results for craters, valleys and slope surfaces are shown in Figure 18, 19, and 20, respectively.

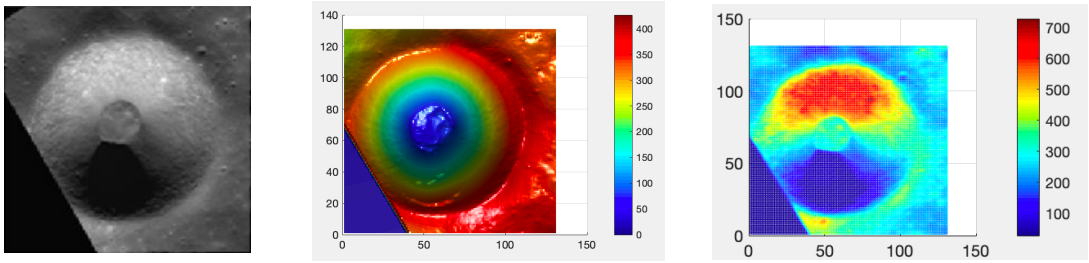

(a) Image (b) Corresponding DEM (c) Detection result

Figure 18. Image, corresponding DEM, detection result of crater

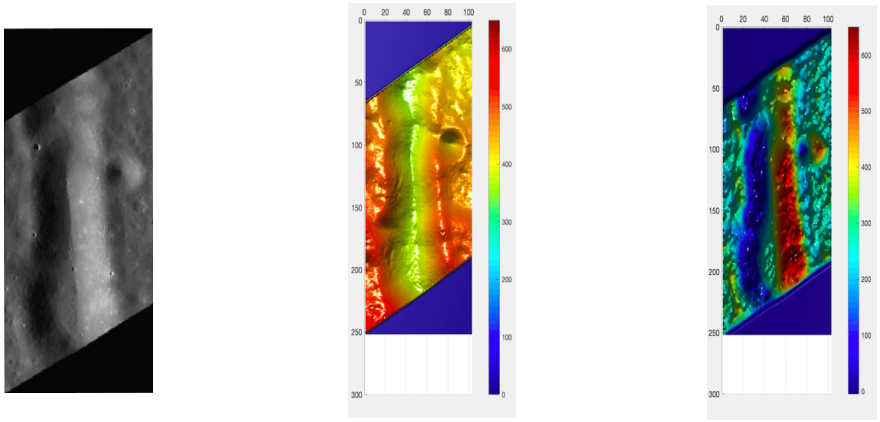

(a) Image (b) Corresponding DEM (c) Detection result

Figure 19. Image, corresponding DEM, detection result of valley

For image of crater, the part facing the direction of the light source is very bright, and the part facing away from the light source is very dark. Since the image of crater has such feature, and SfS recovers shape based on intensity values, the recovered height result also has similar feature, that the height result of the part facing the light source direction is very high, and the height result of the part facing away from the light source direction is very low. Although the recovered result is not accurate, the craters and non-crater parts can be clearly distinguished. Small craters can also be detected.

The result of valley is similar to the crater. SfS cannot recover the shadow parts and the height result is not accurate. But overall, it is easy to distinguish the location of the valleys from the detection result.

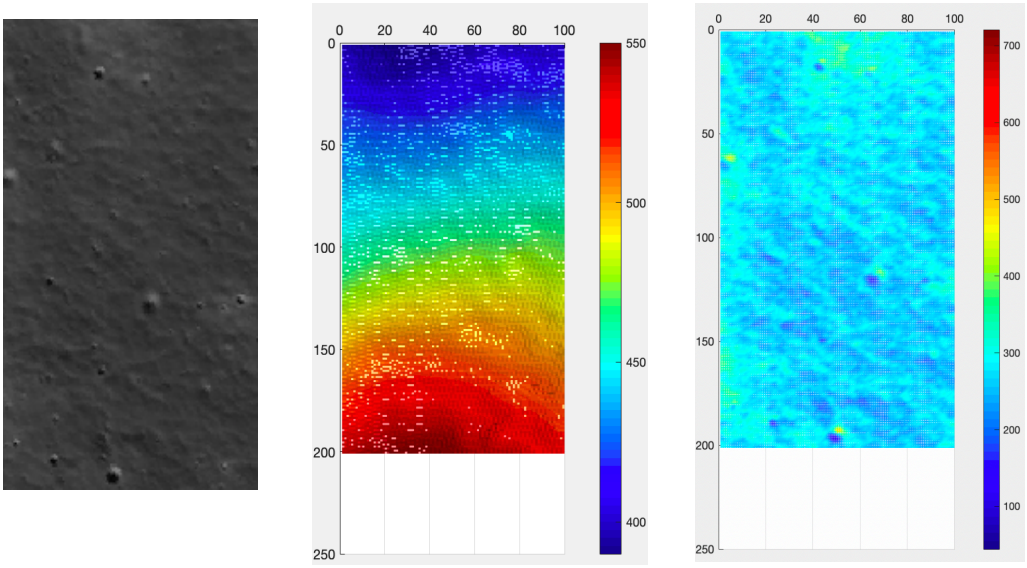

(a) Image (b) Corresponding DEM (c) Detection result

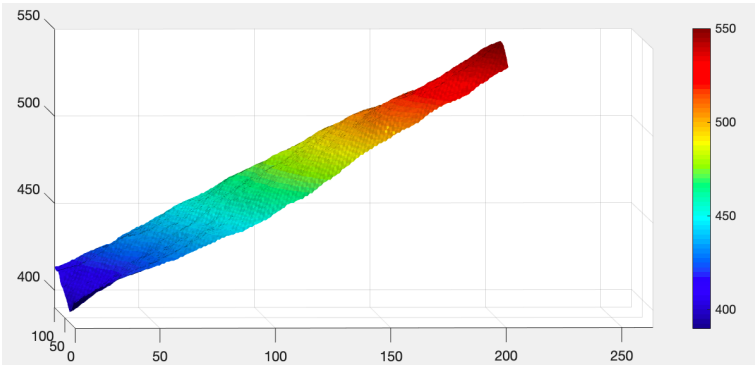

(d) DEM viewing from side

Figure 20. Image, corresponding DEM, detection result of slope surface

For slope surfaces, it cannot be detected by current method. According to DEM (Figure20 (b)), the overall terrain of this part should be a slope surface that height is constantly changing. But in the detection result (Figure20 (c)), this slope change did not be detected by SfS, it shows a relatively flat plane except for some small craters. This is because that, except for these small craters, the intensity values of this part change in a small range, and the intensity change between adjacent points is very small. Since SfS recovers shape based on the intensity value of pixels and the change between adjacent pixels, it cannot detect such slope surface.

At first, we considered that this small intensity value change between pixels may be related to the direction of the light source. When the light source direction is consistent

with the descent direction of the slope when imaging, it may result in a very insignificant change in brightness. So we found some images of slope surfaces, that the light source direction is perpendicular, parallel, or have a certain degree to the descent direction of the slope surface. However, the brightness distribution change for slope surfaces are all small for different situations.

If the image contains slope surface information, the change in brightness value should correspond to the change in the height of this slope surface. But in fact, by observing the image of slope surface (Figure20 (a)), it is impossible even for human eye to find out that this part is actually a slope surface but not a plain. There is not enough information provided by a single image, therefore only using SfS cannot recover the shape of slope surfaces. In order to detect slope surfaces, additional shape information is required.

4 SfS combined with low resolution DEM

In last chapter, we performed experiments using SfS with Hapke model and analyzed the detection results. Then came to the conclusion that the information provided by a single image is not enough to reconstruct the slope surfaces. In order to do this, additional shape information is required.

In this chapter, we consider a method that incorporate a low-resolution DEM into SfS algorithm. Using a single image and low-resolution DEM as the input to recover the shape.

4.1 Related works

Several SfS combined with low-resolution DEM algorithms have been proposed and developed.

Barron and Malik [25] have proposed a method that recover the albedo and shape simultaneously using models normally reserved for natural image statistics. In their works, the albedo parameter is written as a function of surface shape and is optimized toward certain statistical properties. Then they built up an optimization problem that optimizes over the Laplacian pyramid representation of depth, to maximize the likelihood of a prior over the Gaussian pyramid representation of the albedo implied by depth. The experiment results show that their algorithm can produce a reliable and detailed depth result. However, it requires training datasets, which limits its application.

Grumpe et al.'s method [26] separates shape and albedo and optimizes them alternately. The surface shape is recovered by the constraint built by input low-resolution DEM, and the albedo is optimized by a low-pass algorithm to obtain low-frequency information. They introduced a constraint built by the input DEM. This DEM constraint requires the low-pass component of a group of surface gradients to approach with their counterparts in the input low-resolution DEM, that is, the pair of surface gradients which is closest to gradients calculated from DEM is searched.

Then this DEM constraint is combined with brightness constraint and integrability constraint to construct an energy function to recover the surface shape. Their method is able to recover the surface shape on the basis of ensuring the overall terrain changes comply with the terrain given by the input DEM. And since no training sets are required, it is easier to perform.

4.2 Proposed method

We adopt a similar DEM constraint as Grumpe et.al introduced [26], and proposed a new SfS algorithm that combines the linear approach and minimization approach. The linear approach which has fast calculation ability is used to obtain the preliminary height result, and then the minimization method is applied to optimize this preliminary height result and make sure that the detection result complies with the general geometry given by the input low-resolution DEM. For the minimization approach, here no longer using the iterative scheme to compute surface gradients and depth iteratively, but instead using a heuristic algorithm only to optimize the depth result obtained in the previous step. The flow chart of our method is shown in Figure 21. It works in several steps.

(1) The inputs of this method are a low-resolution DEM and a single image (high resolution). Since the resolution of the input image and the DEM are different, it's necessary to use the pyramid hierarchical algorithm to decompose the input image to obtain images in different resolutions. Then the image is resampled to fit to the grid resolution of the DEM.

(2) At each level of the pyramid, the resampled image and resampled DEM are first used to estimate the reflectance parameter for each pixel. Then the linear method is applied to obtain the preliminary depth result, and the minimization constraint is used to optimize this detection result. The refined depth result of current level is generated in this step.

(3) The refined DEM of previous level is up-sampled and taken as the input for the next level, and the same processes in (2) are performed until the depth result reaches the same resolution as the input image. Finally, a refined pixel-level resolution depth result is produced.

Detailed procedures are described in the following sections.

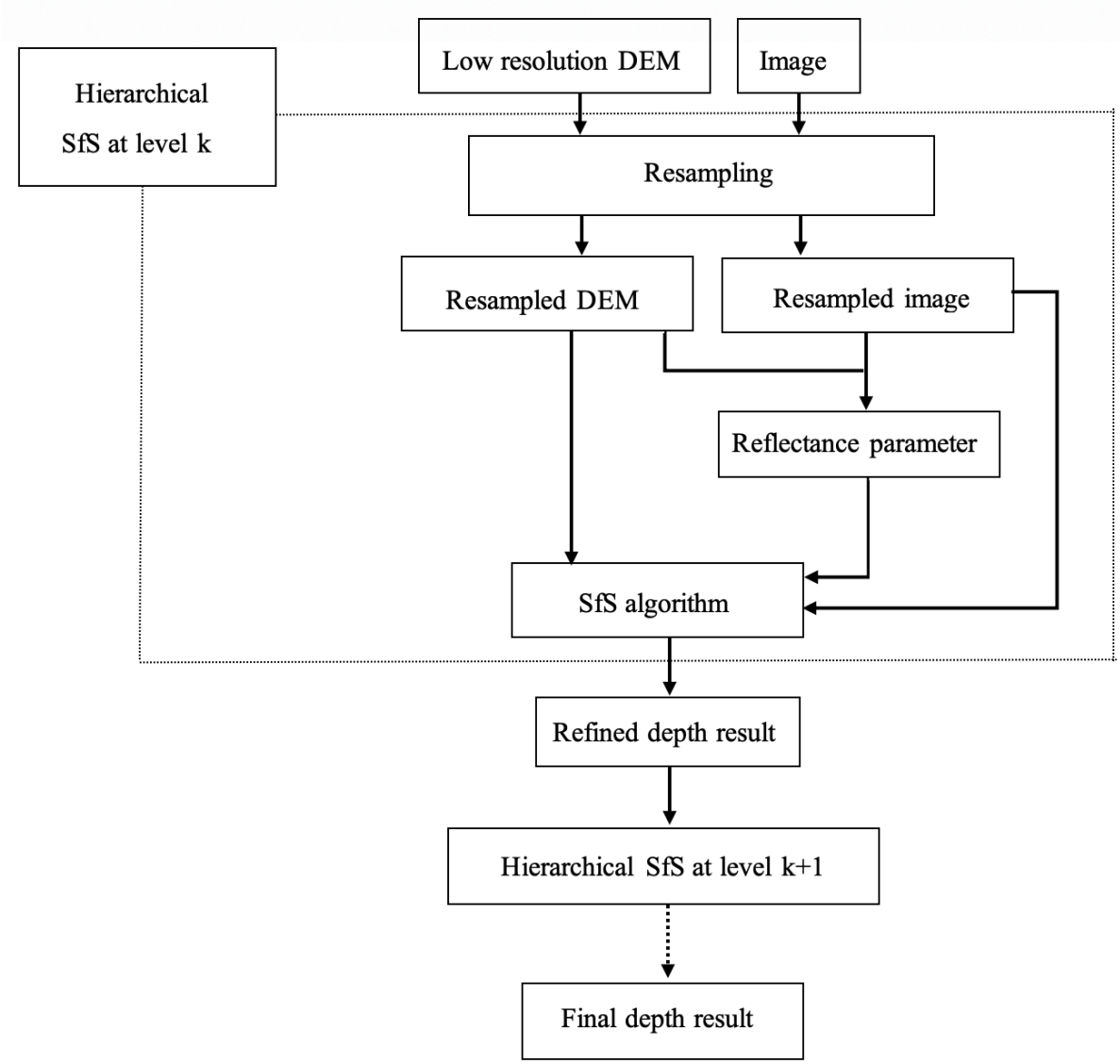

Figure 21. Flow chart of proposed method

4.2.1 Reflectance parameter estimation

The Hapke reflectance model contains several different parameters describing the surface properties, and it is impossible to estimate all parameters. Therefore, here using the simplified Hapke model introduced in section 3.2.2. The reflectance function is expressed as,

$$R_{Hapke} = \frac{w}{4\pi} \frac{\cos i}{\cos i + \cos e} \frac{1+2\cos i}{1+2\gamma\cos i} \frac{1+2\cos e}{1+2\gamma\cos e} \quad (4.1)$$

For this simplified Hapke model, only one parameter, single-scattering albedo w needs to be estimated. According to the image-irradiance equation ($I = R(p,q)$), w can be calculated.

At each level of hierarchy, the w parameter is estimated using input DEM and image, then it is used for surface shape reconstruction. After depth result of current level is obtained, the depth result is up-sampled and used to compute the subsequent new set of w.

4.2.2 Shape reconstruction

The surface shape is reconstructed by two strategies: using the linear method proposed by Tsai and Shah in combination with the simplified Hapke model to obtain preliminary depth result, then optimizing this preliminary depth result through DEM constraint. This section introduces the first one.

The simplified Hapke model is expressed as,

$$R(p,q) = \frac{w}{4\pi}\frac{C_e F_s}{C_s F_e + C_e F_s}\frac{FC_s + 2F_s}{FC_s + 2\gamma F_s}\frac{FC_e + 2F_e}{FC_e + 2\gamma F_e} \tag{4.2}$$

where

$$C_s = \sqrt{1 + p_s^2 + q_s^2} \tag{4.3}$$

$$C_e = \sqrt{1 + p_e^2 + q_e^2} \tag{4.4}$$

$$F_s = 1 + pp_s + qq_s \tag{4.5}$$

$$F_e = 1 + pp_e + qq_e \tag{4.6}$$

$$F(p,q) = \sqrt{1 + p^2 + q^2} \tag{4.7}$$

$$\gamma = \sqrt{1 - w} \tag{4.8}$$

Then the image-irradiance equation ($I = R(p,q)$) can be rewritten as:

$$f = R\left(p_{i,j}, q_{i,j}\right) - I_{i,j} = 0 \tag{4.9}$$

Using finite differences to linearize f, it yields,

$$\begin{aligned} f = R\left(p_{i,j}, q_{i,j}\right) + \alpha\left(\frac{\partial R}{\partial p}\cdot\left(\frac{\partial p}{\partial x} + \frac{\partial p}{\partial y}\right) + \frac{\partial R}{\partial q}\cdot\left(\frac{\partial q}{\partial x} + \frac{\partial q}{\partial y}\right)\right) \\ -I(i,j) - \alpha\left(I_x(i,j) + I_y(i,j)\right) \end{aligned} \tag{4.10}$$

where

$$\frac{\partial R}{\partial p} = PA \cdot \frac{C_s \cdot F + 2F_s}{C_s \cdot F + 2\gamma F_s} \cdot \frac{C_e \cdot F + 2F_e}{C_e \cdot F + 2\gamma F_e} + PB \cdot \frac{C_e \cdot F_s}{C_e \cdot F_s + C_s F_e} \cdot \frac{C_e \cdot F + 2F_e}{C_e \cdot F + 2\gamma F_e} + PC \cdot \frac{C_e \cdot F_s}{C_e \cdot F_s + C_s F_e} \cdot \frac{C_s \cdot F + 2F_s}{C_s \cdot F + 2\gamma F_s}$$

(4.11)

$$PA = \frac{C_e C_s p_s (q_e q + 1) - C_e C_s p_e (q_s q + 1)}{(C_e F_s + C_s F_e)^2} \tag{4.12}$$

$$PB = \frac{2(\gamma - 1) C_s p F_s + 2(1 - \gamma) C_s p_s F^2}{F(C_s F + 2\gamma F_s)^2} \tag{4.13}$$

$$PC = \frac{2(\gamma - 1) C_e p F_e + 2(1 - \gamma) C_e p_e F^2}{F(C_e F + 2\gamma F_e)^2} \tag{4.14}$$

$$\frac{\partial R}{\partial q} = QA \cdot \frac{C_s \cdot F + 2F_s}{C_s \cdot F + 2\gamma F_s} \cdot \frac{C_e \cdot F + 2F_e}{C_e \cdot F + 2\gamma F_e} + QB \cdot \frac{C_e \cdot F_s}{C_e \cdot F_s + C_s F_e} \cdot \frac{C_e \cdot F + 2F_e}{C_e \cdot F + 2\gamma F_e} + QC \cdot \frac{C_e \cdot F_s}{C_e \cdot F_s + C_s F_e} \cdot \frac{C_s \cdot F + 2F_s}{C_s \cdot F + 2\gamma F_s}$$

(4.15)

$$QA = \frac{C_e C_s q_s (p_e p + 1) - C_e C_s q_e (p_s p + 1)}{(C_e F_s + C_s F_e)^2} \tag{4.16}$$

$$QB = \frac{2(\gamma - 1) C_s q F_s + 2(1 - \gamma) C_s q_s F^2}{F(C_s F + 2\gamma F_s)^2} \tag{4.17}$$

$$QC = \frac{2(\gamma - 1) C_e q F_e + 2(1 - \gamma) C_e q_e F^2}{F(C_e F + 2\gamma F_e)^2} \tag{4.18}$$

Taking the Taylor expansion of function f about $z_{i,j} = z_{i,j}^{n-1}$ up through the first order terms to obtain,

$$0 = f\left(z_{i,j}\right) \approx f\left(z_{i,j}^{n-1}\right) + \left(z_{i,j} - z_{i,j}^{n-1}\right) \frac{\partial f}{\partial z_{i,j}} \left(z_{i,j}^{n-1}\right) \tag{4.19}$$

For $z_{i,j} = z_{i,j}^{n}$ (the depth at n-th iteration), there is,

$$z_{i,j}^{n} = z_{i,j}^{n-1} + \frac{-f(z_{i,j}^{n-1})}{\frac{\partial f}{\partial z_{i,j}}(z_{i,j}^{n-1})} \tag{4.20}$$

The height value given by low resolution DEM is used as initial values for z, then the preliminary depth result is obtained using above equation iteratively.

4.2.3 Optimization

In the previous section, the linear method is used to obtain the preliminary depth result. Then constructing an energy function to add the known surface shape to optimize this depth result. For the preliminary depth result, even using the input low

resolution DEM as initial height value to recover the surface shape, the detection result tends to be flat, the overall terrain change given by input low resolution DEM is lost. Therefore, this input low resolution DEM is first superimposed on preliminary depth result, then it is optimized by minimization method to ensure the depth result conform to the overall geometry given by the input DEM.

The DEM constraint we use is also built by the input DEM, but unlike Grumpe et al.'s method, we use the depth value instead of surface gradients to build constraint. This constraint requires the low-pass component of depth value to approach with the input DEM. It is expressed as,

$$\begin{aligned} E_z &= \iint (G(z) - G(z_{DEM}))^2 dxdy \\ &= \iint (g_{\sigma_{DEM}} \circ z - g_{\sigma_{DEM}} \circ z_{DEM})^2 dxdy \end{aligned} \tag{4.21}$$

where $g_{\sigma_{DEM}}$ is a Gaussian filter of width σ_{DEM}, $\circ$ is the correlation operator.

The energy function is built by the weighted sum of above constraint and integrability constraint (equation (2.9)), which is

$$\begin{aligned} E_{depth} &= E_{int} + \tau E_Z = \iint F\big(z, z_x, z_y\big) dxdy \\ F\big(z, z_x, z_y\big) &= \Big((z_x - p)^2 + \big(z_y - q\big)^2\Big) + \tau (g_{\sigma_{DEM}} \circ z - g_{\sigma_{DEM}} \circ z_{DEM})^2 \end{aligned} \tag{4.22}$$

It can also generate a Euler equation,

$$p_x + q_y = z_{xx} + z_{yy} - \tau (G(z) - G(z_{DEM})) \cdot \frac{\partial G(z)}{\partial z} \tag{4.23}$$

where $\frac{\partial G(z)}{\partial z} = \frac{z_x \cdot \frac{\partial}{\partial x} G(z) + z_y \cdot \frac{\partial}{\partial y} G(z)}{z_x^2 + z_y^2}$.

It is possible to obtain the iterative formula for z using the above Euler equation, however it is quite time-consuming. Therefore, here applying a heuristic algorithm to find the locally optimal choice by minimizing the absolute value of the right-hand side of equation (4.23) for a given z. The heuristic algorithm works in several steps.

(1) The initial values for z are taken from the preliminary depth result. The order of all pixels is set to 1, indicating that the depth of this pixel is admissible for changes.

(2) For all pixels (i, j), $z_{i,j}$ is increased by h (h is set according the the height range of DEM). If the error value (the absolute value of the right-hand part of the equation (4.23) decreased, the new $z_{i,j}$ value is saved. Otherwise, the $z_{i,j}$ is decreased by h, and this new $z_{i,j}$ value is saved only if the error value decreases. If the error value increases, the order of $z_{i,j}$ is changed to 0, indicating that the depth of this pixel is not admissible for change anymore.

(3) The above procedure is continued until the order of all pixels become 0 or the maximum number of loops is reached.

A refined depth result is generated after optimization. Then it is up-sampled and taken as input for the next level of hierarchy until the resolution of depth result reaches the resolution of the image.

4.3 Experimental analysis

4.3.1 Datasets

Three datasets were presented and used in this research.

(1) Lunar Reconnaissance Orbiter Camera (LROC) images. LROC is a system of three cameras mounted on the Lunar Reconnaissance Orbiter (LRO) that capture high resolution images of the lunar surface. It consists of two Narrow Angle Cameras (NAC) and one Wide Angle Camera (WAC). Here using the LRO NAC images as the input images. The LRO NAC images have high resolution, 0.5—2 meters per pixel, they can provide very detailed lunar terrain. The images were obtained from the LROC Archive [20]. The details of selected images are listed in Table 4.

(2) Digital elevation models (DEMs) provided by the LROC RDR (Reduced Data Record) products. RDR is a product that made from one or multiple images that are processed and reduced for the purpose of, for example, making a high resolution global digital elevation model created with stereo observations. Here using the DEMs provided by RDR product for the comparison purposes. These DEMs have high resolution (~2m/pixel), and they were also obtained from the LROC Archive [20].

(3) Low resolution DEM provided by SLDEM2015. The SLDEM2015 data product is the DEM created by the Lunar Orbiter Laser Altimeter (LOLA) data and images from stereo SELENE Terrain Camera (TC) datasets. The resolution is near 512 pixels per degree, equivalent to 60 meters per pixel near the equator, and better at higher latitudes. The SLDEM2015 data were obtained from the website in reference 27.

Table 4. Details of LROC images used in the experiments

	Dataset 1	Dataset 2
Image ID	M173246166	M160139273
Resolution	2 m/pixel	2 m/pixel
Covered longitude	308.48 — 308.75°	332.03 — 332.19°
Covered latitude	43.60 — 44.55°	-1.99 — -2.93°
Sun azimuth	121.85°	184.41°
Incidence angle	49.04°	50.03°
Emission angle	16.32°	16.28°
Phase angle	43.7°	64.1°
Image size used in the experiments	350 x 228 pixels	970 x 940 pixels

The LROC image and low resolution DEM obtained from SLDEM2015 are used as the input to reconstruct three dimensional terrain of selected area. Then the detection result is compared with DEM provided by LROC RDR product to analyze the performance of the algorithm.

4.3.2 Experimental results for dataset 1

The image of dataset 1 is selected from the LROC image with ID number M173246166. It contains an area of 350 x 228 pixels with a resolution of 2m/pixel. This input image is shown in Figure 22(a). According to the latitude and longitude information for this LROC image (Table 4), the corresponding area is selected from the SLDEM2015 data to use as the input low-resolution DEM. It covers the testing region with only 12 x 8 pixels, with a resolution of 60m/pixel, as shown in Figure 22(b).

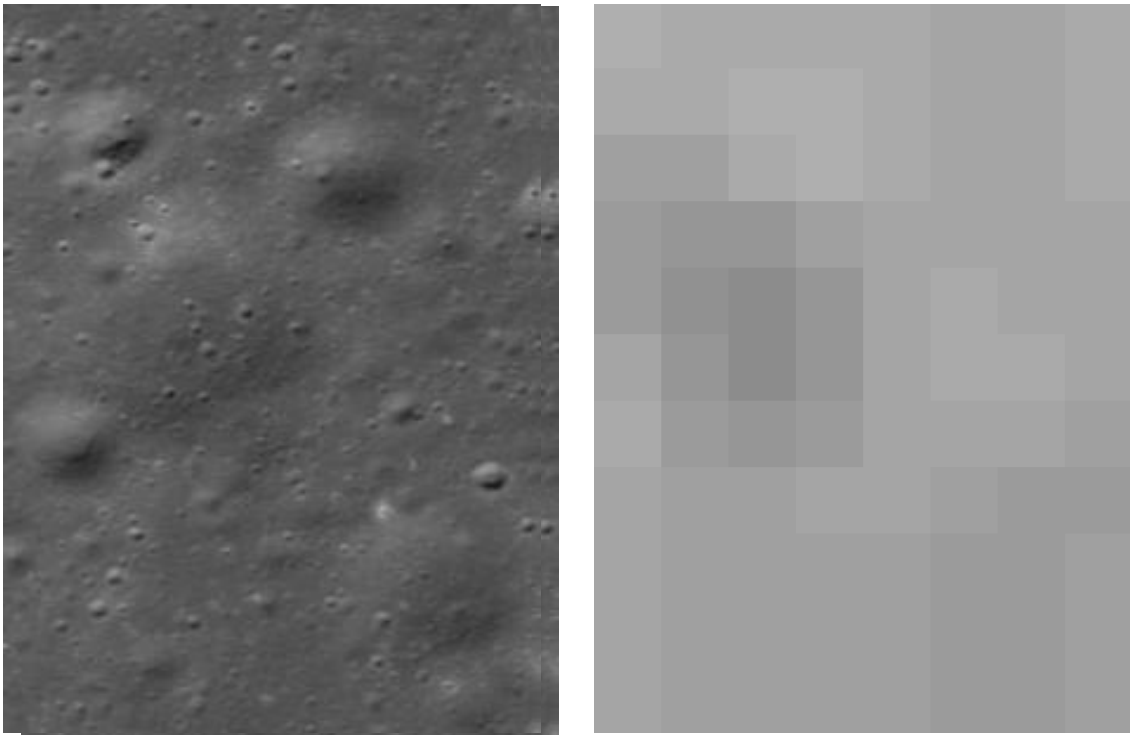

(a) Input image of dataset 1 (2m/pixel)

(b) Input low resolution DEM of dataset 1 (60m/pixel)

Figure 22. Input image and low resolution DEM for dataset 1

Using the image and low-resolution DEM as input, and applying our SfS algorithm to obtain the detection result, which is shown in Figure 23 (a). Another DEM (referred to as LROC DEM) used for comparison is shown in Figure 23(b). Its resolution is the same as the input image, which is 2m/pixel.

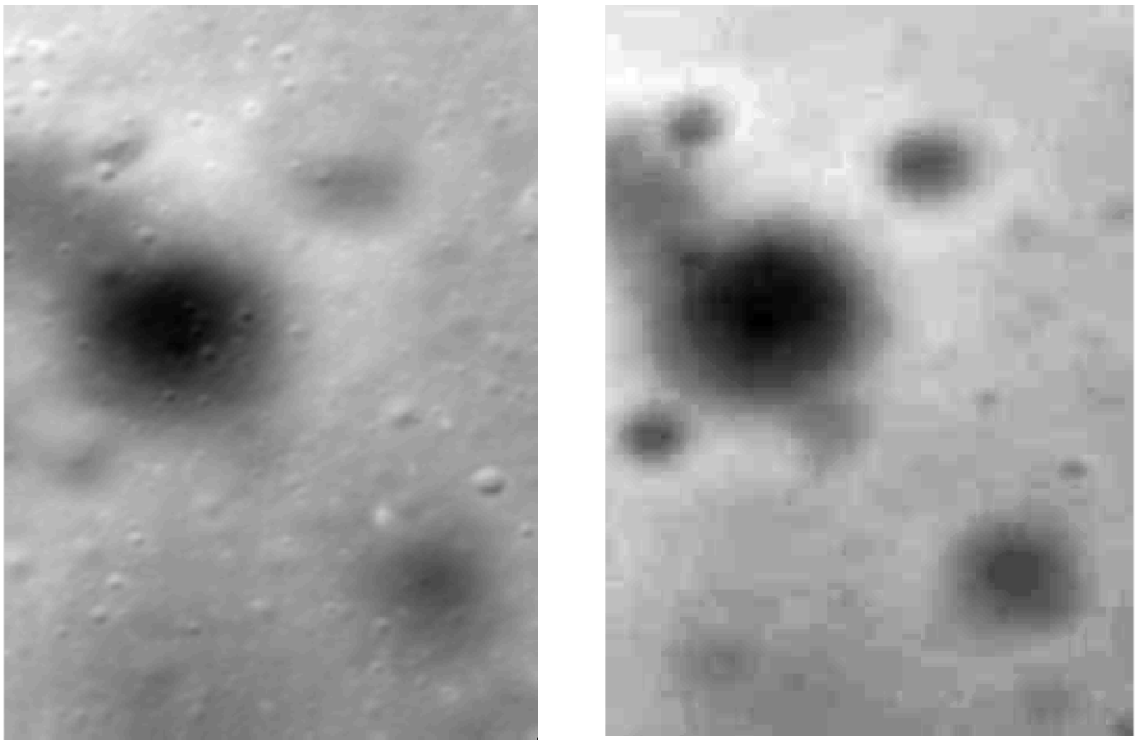

(a) Detection result (2m/pixel) (b) LROC DEM used for comparison (2m/pixel)

Figure 23. Detection result and LROC DEM for dataset 1

Figure 24 gives the 3D view of the input low resolution DEM, detection result, and reference LROC DEM.

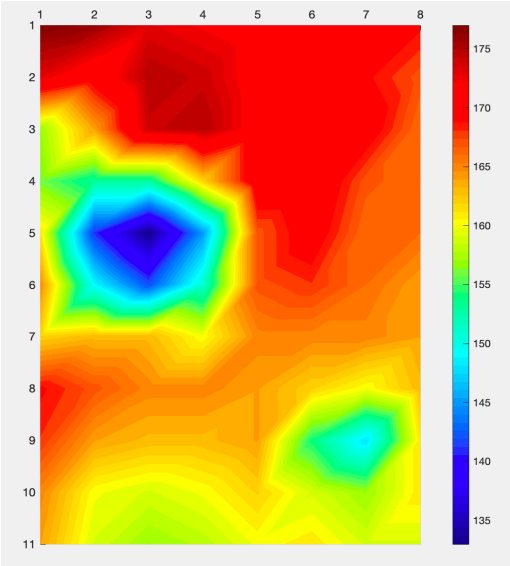

(a) 3D view of input low resolution DEM

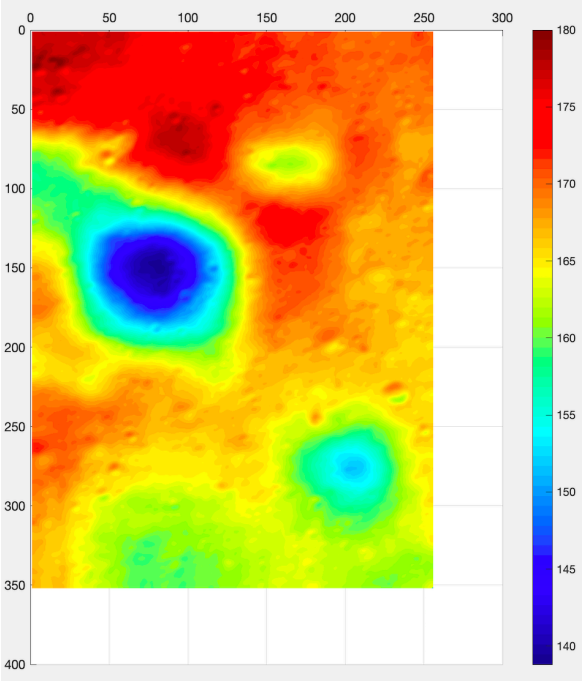

(b) 3D view of the detection result

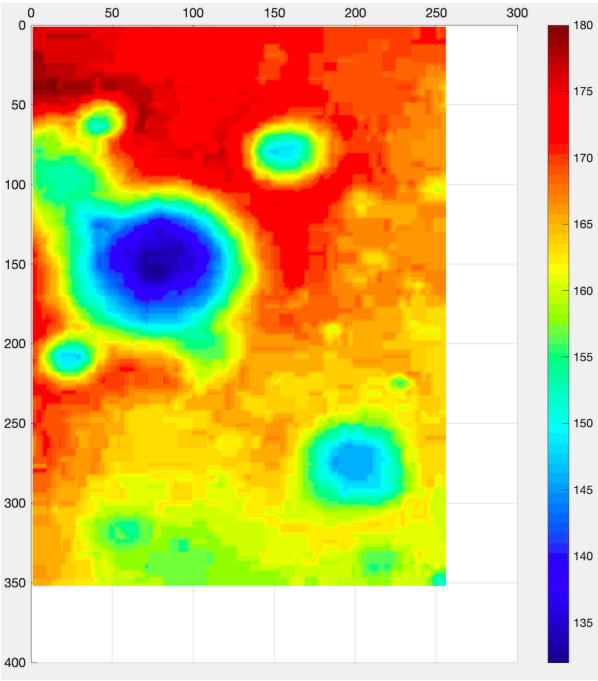

(c) 3D view of the LROC DEM

Figure 24. 3D view of the input low resolution DEM, detection result and reference LROC DEM for dataset 1

The overall terrain of dataset 1 is a slope surface with obvious inclination change. There are two large craters on it, and several relatively small craters around the crater at upper left corner.

The key topographical structure of this region (the overall slope change and two large craters) represented by LROC DEM are well preserved in the input low resolution DEM. Therefore, it allows the algorithm to converge to the detection result with high correspondence with the LROC DEM, the overall terrain change is well recovered. Especially for the slope surface changes that failed to be recovered only using SfS, they can be recovered well after incorporating the low resolution DEM as constaint.

For the details, it can be seen from the comparison in Figure 24 that the algorithm can recover some details that are not presented in the LROC DEM. Since SfS recovers the surface shape based on the intensity value of pixels, the detailed small features apparent in the input image can be well recovered. For example, there are a few small craters inside the big crater at the upper left corner, as shown in Figure 25 (a). These

small craters are recovered in the detection result (Figure 25 (b)), while there is no such information in the LROC DEM (Figure 25 (c)).

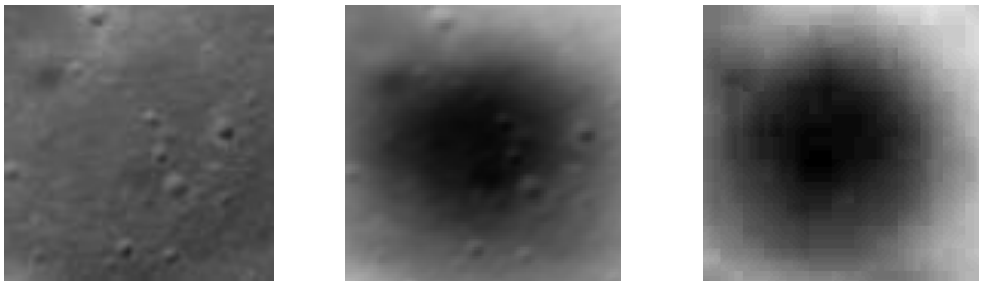

(a) Image (b) Detection result (c) LROC DEM

Figure 25. Image, detection result and LROC DEM for details in dataset 1

In order to analyze the detection result objectively and qualitatively, the detection result was first normalized to the same height range with LROC DEM, then compared with LROC DEM to calculate the height value error. Table 5 gives the average absolute height error value, maximum height error and standard deviation of absolute height error for dataset 1. The average absolute height error is within 3 meters and the standard deviation of absolute height error is within 2 meters, which indicates that the algorithm can recover shape very well. However, the maximum height error value is quite large, about 20 meters.

Table 5. Statistical analysis of experimental dataset 1.

	Average of absolute height error (m)	Maximum height error (m)	Standard deviation of absolute height error (m)
Dataset 1	2.7262	20.2859	1.5647

Figure 26 gives the absolute height error value map, which allows us to visually observe locations where the large error exists. It can be seen that the height error mainly exists in several craters. Especially these three relatively small craters near the big crater at the upper left corner have larger error values. This is because the algorithm recovers surface shape based on input low resolution DEM, and in the optimization stage of the preliminary depth result, we directly use the height value of

low resolution DEM as a constraint to optimize the detection result. Therefore, the overall terrain of the final detection result complies with the terrain given by the input DEM. If the overall geometry in low resolution DEM is not preserved as well as the LROC DEM, it will lead to errors in the results. This can be improved by using other information obtained from the input low resolution DEM (eg. estimated reflectance, surface gradients) as constraints instead of directly using height values to optimize depth result.

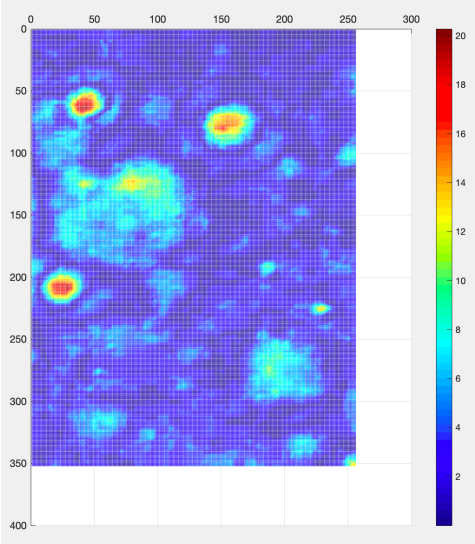

Figure 26. Absolute height error map for dataset 1

4.3.3 Experimental results for dataset 2

The image of dataset 2 is selected from the LROC image with ID number M160139273. It contains an area of 970 x 940 pixels with a resolution of 2m/pixel. The input image is shown in Figure 27(a). According to the latitude and longitude information for this LROC image (Table 4), the corresponding area is selected from the SLDEM2015 data to use as the input low-resolution DEM. It covers the testing region with 32 x 31 pixels, with a resolution of 60m/pixel, as shown in Figure 27(b).

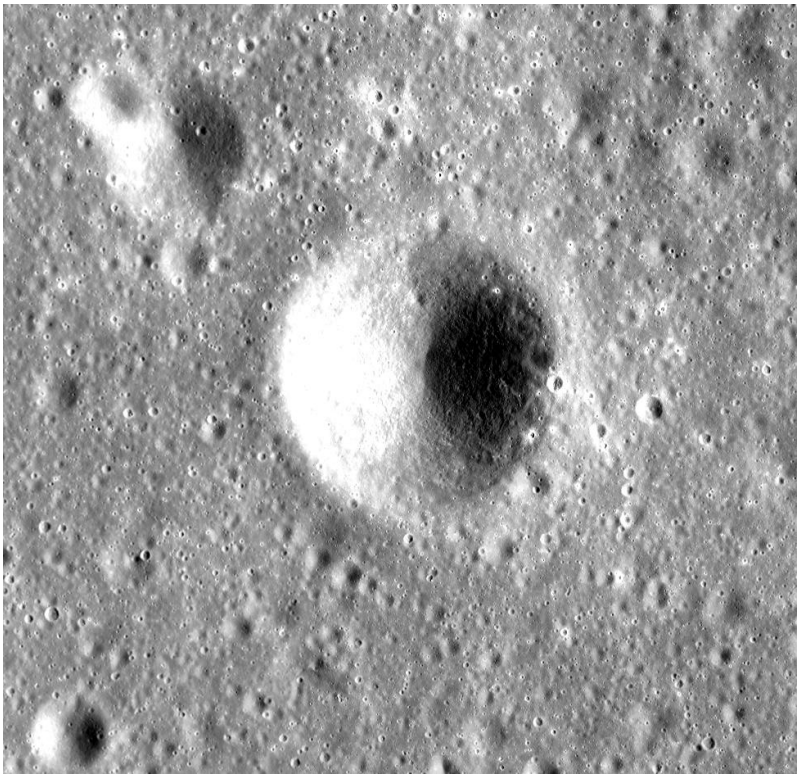

(a) Input image of dataset 2 (2m/pixel)

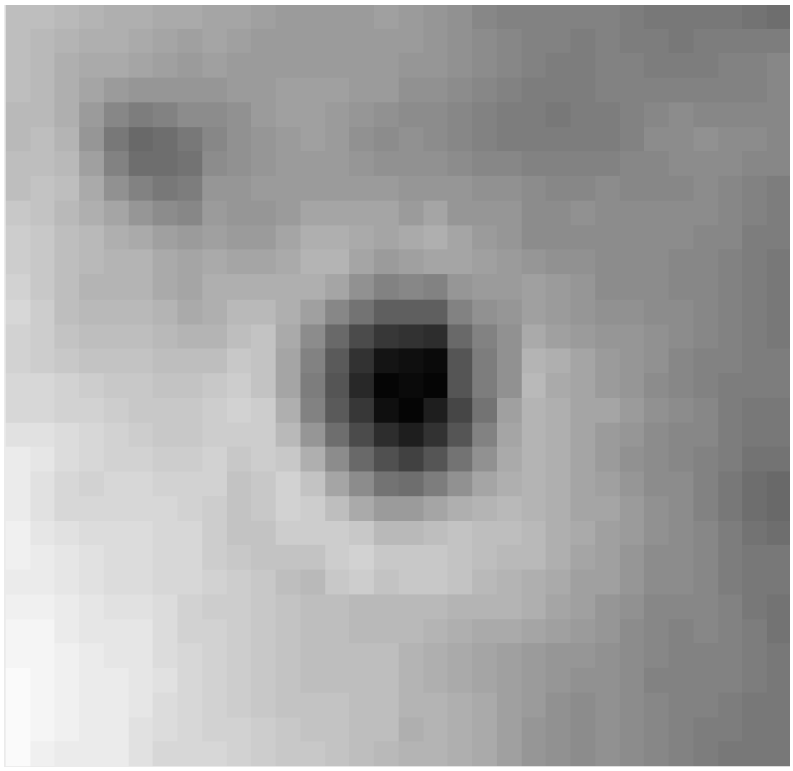

(b) Input low resolution DEM of dataset 2 (60m/pixel)

Figure 27. Input image and low resolution DEM for dataset 2

Applying the algorithm to obtain the detection result, which is shown in Figure 28 (a). LROC DEM used for comparison is shown in Figure 28(b). Figure 29 gives the 3D view of the input low resolution DEM, detection result, and reference LROC DEM.

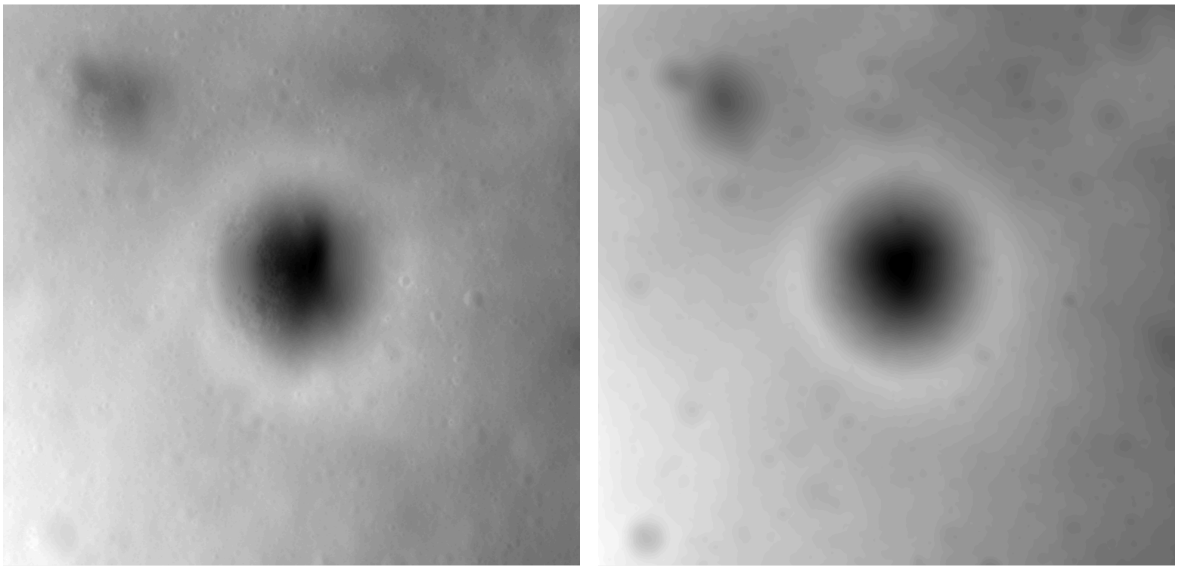

(a) Detection result (2m/pixel) (b) LROC DEM used for comparison (2m/pixel)

Figure 28. Detection result and LROC DEM for dataset 2

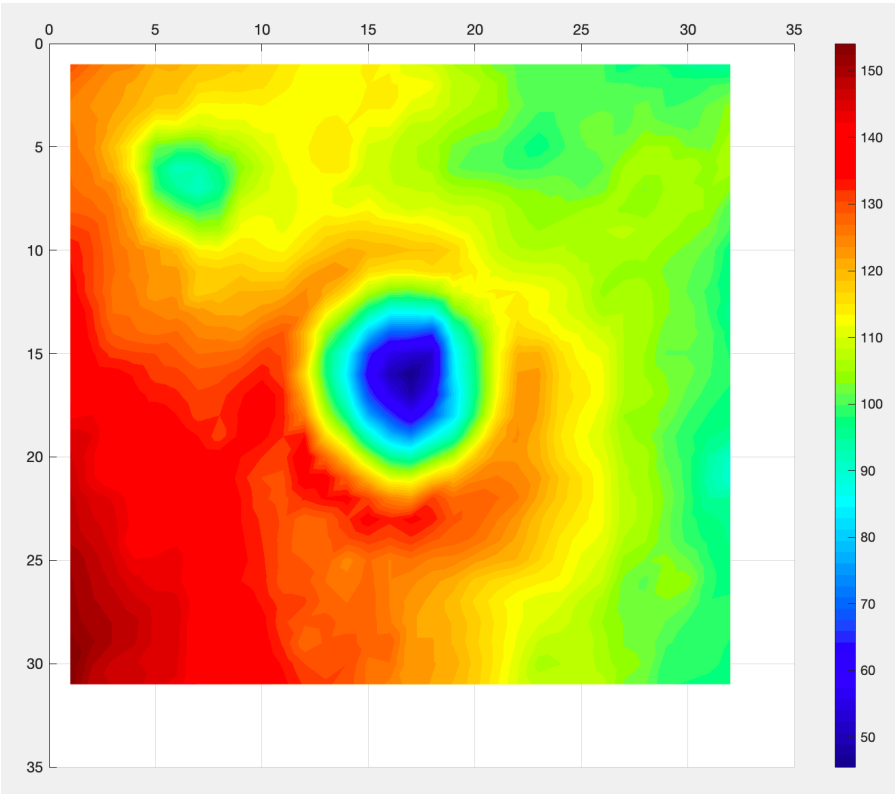

(a) 3D view of input low resolution DEM

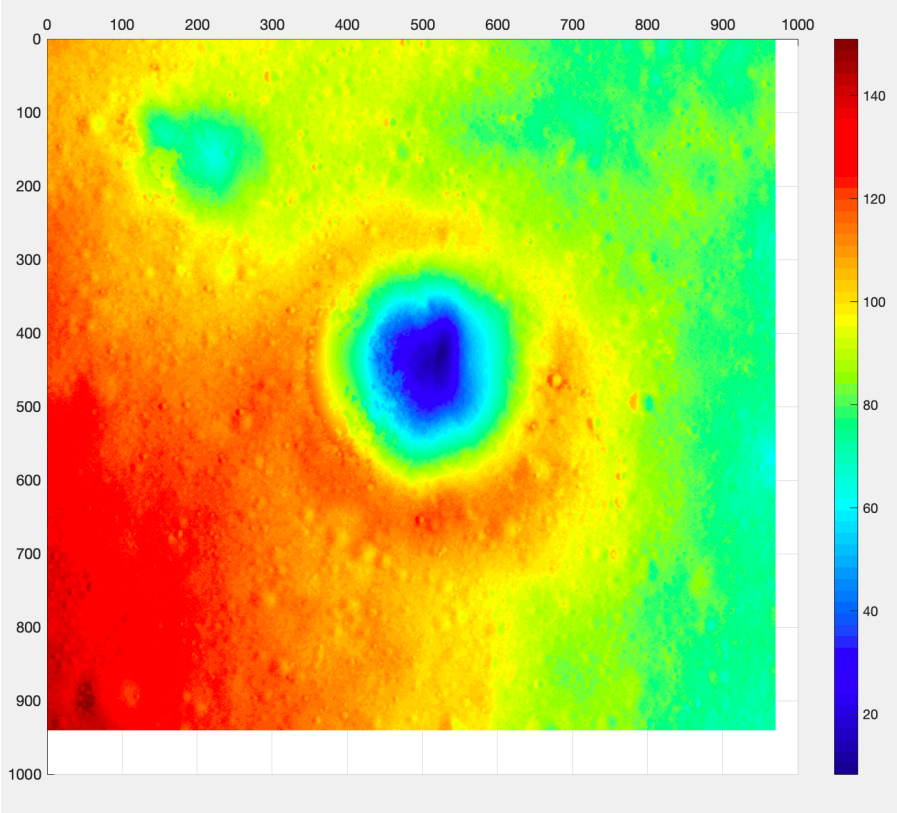

(b) 3D view of the detection result

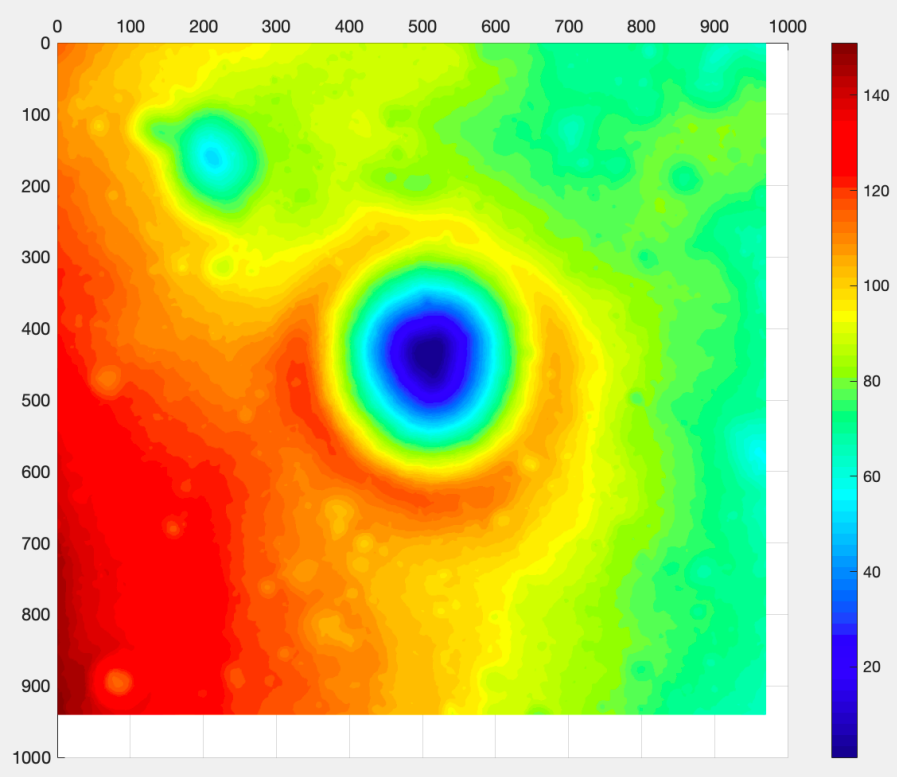

(c) 3D view of the LROC DEM

Figure 29. 3D view of the input low resolution DEM, detection result and reference LROC DEM for dataset 2

Compared to dataset 1, dataset 2 is more complex and covers much more pixels. There is a large crater located in the center of the image, the height differences between two sides of this crater is very large, which increases the difficulty of recovery. There is also a relatively small crater in the upper left corner, and these topographical structures are well preserved in the low resolution DEM, while the small crater in the lower left corner does not. And there are lots of small craters cover the whole image.

Similar to the detection result of dataset1, since the key topographical structure of this area is well preserved in the low-resolution DEM, the algorithm can recover the overall terrain well, and can also recover the local details which are not preserved in the LROC DEM. Comparing the detection result of current method (Figure 29 (a)) with the detection result in Figure 17 (c) that using only a single image as an input. It can be found that the slope surface changes that failed to be recovered only using information provided by a single image can be recovered well after incorporating the low resolution DEM as constraint.

For qualitative analysis, here giving the height value error between the detection result and the LROC DEM as shown in Table 6. The average absolute height error is about 4 meters and the standard deviation of absolute height error is within 2 meters, which indicates that the algorithm can recover shape very well. However, the maximum height error value is quite large, about 24 meters. Figure 30 gives the absolute height error value map, allows us to visually observe locations where the large error exists.

Table 6. Statistical analysis of experimental dataset 2.

	Average of absolute height error (m)	Maximum height error (m)	Standard deviation of absolute height error (m)
Dataset 2	4.0108	24.2040	1.7420

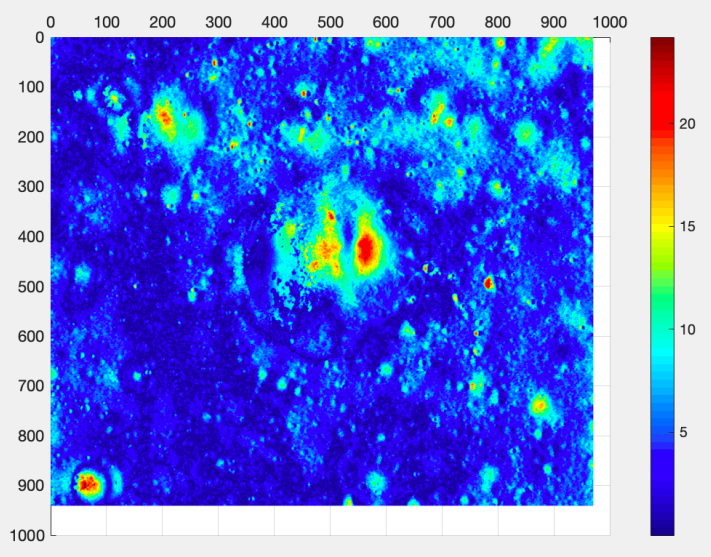

Figure 30. Absolute height error map for dataset 2

It can be seen that the error mainly exists in the large crater located in the center of image, two relatively small craters in the upper left and lower left corners. The height error of these three large craters is caused by the error between the input low resolution DEM and the LROC DEM. As mentioned in section 4.3.2, this problem can be improved by using other information obtained from input DEM rather than height value as constraint.

We performed our algorithm on MacBook Pro with 2.3GHz Core i5 CPU and 8GB memory. And for dataset 2 (970 x 940 pixels), the computation time is 21.15 seconds.

5 Conclusion and future work

5.1 Conclusion

This research proposed a method using Shape from Shading combined with low resolution DEM to reconstruct terrain on planetary surface and estimate slope surfaces.

We first tested four approaches for SfS and analyzed their results. Then we performed experiments using linear method with Hapke reflectance model. The detection results were analyzed, and come to the conclusion that the information provided by a single image is not enough to restore the slope topography, thus additional shape information is needed.

Then we introduced a SfS algorithm combined with low resolution DEM, using image and low resolution DEM as input. First the pyramid hierarchical algorithm is used to decompose the input image to obtain images in different resolutions. At each level of the pyramid, the resampled image and resampled DEM are used to estimate the reflectance parameter, then SfS algorithm is applied to reconstruct surface shape. The depth result of current level is up-sampled and use as the input for next level. Same processes are performed until the depth result reaches the same resolution as the input image. The detection results of two datasets show that after incorporating the low resolution DEM as constraint to recover shape, the algorithm can reconstruct the overall terrain very well and detect detailed small obstacles, the average height error is small.

5.2 Future work

Although proposed method can reconstruct the overall terrain well and the height error is small, there are still some problems that need improvement.

The algorithm uses depth value from input DEM as constraint to reconstruct surface shape, thus the detection result conforms to the overall geometry given by the input

DEM. However, since there are inaccuracies in the input DEM, it may lead to errors in the detection result. For the future work, considering using other information obtained from the input DEM (eg. reflectance function, surface gradients) to construct constraints instead of directly using the height value. This may reduce the error in detection result caused by the inaccuracies of the input DEM.

In the simulation experiments, we used the input low resolution DEMs with 60m/pixel resolution and images with 2m/pixel resolution, and obtained promising results. However, if the resolution difference between image and low resolution DEM is larger, the key geometry information may lost, which leads to inaccuracies in shape. Thus for future work, it is necessary to discuss the suitable range of resolution difference between image and input DEM.

As for calculation time, for dataset 2 (970 x 940 pixels), it took 21.15 seconds. In order to further shorten the calculation time, it is possible to delete pixel points that the intensity value is too high or too low which corresponds to the obvious obstacles, thus reduce the amount of data to shorten the calculation time. Also, it is possible to use DEM that has smaller resolution difference with the input image to reduce the number of usage of SfS algorithm, thereby reducing the calculation time.

In the proposed method, the reflectance parameter of each pixel is estimated using the height value and the intensity value of pixels, and then used for terrain reconstruction. We did not assess the accuracy of reflectance parameter map since there is no available reference reflectance parameter map. And since the height values of the input DEM used in the experiment are relatively accurate, good depth results were obtained. However, if there are large height errors existing in input DEM, it may result in errors in the reflectance parameter map. Therefore, for future work, considering using a piece-wise constant albedo assumption to estimate reflectance parameter for each pixel to reduce the influence from the inaccuracies of the input DEM.

Currently, we take a single image and a low resolution DEM as input and use the Shape from Shading algorithm to recover the surface shape. For the future work, it is possible to include more image information. For example, considering the multi-views Shape from Shading method, using multiple images and a low resolution DEM as inputs to restore terrain.

Publication

- Mengzhi Di, Tatsuaki Hashimoto, "A Study on Slope Estimation of Planetary Surface." The 32nd International Symposium on Space Technology and Science & the 9th Nano-Satellite Symposium, 2019. (Oral)

References

[1] Grant, John A., et al. "Selecting landing sites for the 2003 Mars Exploration Rovers." *Planetary and Space Science* 52.1-3 (2004): 11-21.

[2] Li, Shuang, Xiuqiang Jiang, and Ting Tao. "Guidance summary and assessment of the Chang'e-3 powered descent and landing." *Journal of Spacecraft and Rockets* 53.2 (2016): 258-277.

[3] Wu, Weiren, et al. "Autonomous hazard detection and avoidance guidance method for soft lunar landing." *Science China Press* 45.8 (2015): 1046r-1059 (in Chinese).

[4] Matthies, Larry, et al. "Stereo vision and shadow analysis for landing hazard detection." *2008 IEEE International Conference on Robotics and Automation*. IEEE, 2008.

[5] Leroy, Bertrand, et al. "Crater detection for autonomous landing on asteroids." *Image and Vision Computing* 19.11 (2001): 787-792.

[6] Woicke, Svenja, and Erwin Mooij. "Passive hazard detection for planetary landing." *AIAA guidance, navigation, and control conference*. 2016.

[7] Johnson, Andrew, James Montgomery, and Larry Matthies. "Vision guided landing of an autonomous helicopter in hazardous terrain." *Proceedings of the 2005 IEEE International Conference on Robotics and Automation*. IEEE, 2005.

[8] Zhang, Ruo, et al. "Shape-from-shading: a survey." *IEEE transactions on pattern analysis and machine intelligence* 21.8 (1999): 690-706.

[9] Ikeuchi, Katsushi, and Berthold KP Horn. "Numerical shape from shading and occluding boundaries." *Artificial intelligence* 17.1-3 (1981): 141-184.

[10] Lee, Kyoung Mu, and C-CJ Kuo. "Shape from shading with a linear triangular element surface model." *IEEE Transactions on Pattern Analysis and Machine Intelligence* 15.8 (1993): 815-822.

[11] Horn, Berthold KP. "Height and gradient from shading." *International journal of*

computer vision 5.1 (1990): 37-75.

[12] Zheng, Qinfen, and Rama Chellappa. "Estimation of illuminant direction, albedo, and shape from shading." *Proceedings. 1991 IEEE Computer Society Conference on Computer Vision and Pattern Recognition*. IEEE, 1991.

[13] Horn, B. K. P. "A method for obtaining the shape of a smooth opaque object from one view." *Massachusetts Institute of Technology, Cambridge, MA* (1970).

[14] Bichsel, Martin, and Alex P. Pentland. "A simple algorithm for shape from shading." *Proceedings 1992 IEEE Computer Society Conference on Computer Vision and Pattern Recognition*. IEEE, 1992.

[15] Pentland, Alex P. "Local shading analysis." *IEEE Transactions on Pattern Analysis & Machine Intelligence* 2 (1984): 170-187.

[16] Lee, Chia-Hoang, and Azriel Rosenfeld. "Improved methods of estimating shape from shading using the light source coordinate system." *artificial Intelligence* 26.2 (1985): 125-143.

[17] Pentland, Alex. "Shape information from shading: a theory about human perception." *Second International Conference on Computer Vision*. IEEE, 1988.

[18] Ping-Sing, Tsai, and Mubarak Shah. "Shape from shading using linear approximation." *Image and Vision computing* 12.8 (1994): 487-498.

[19] SELENE Data Archive, http://darts.isas.jaxa.jp/planet/pdap/selene/index.html.ja/ (accessed June 21, 2018).

[20] LROC Archive: http://lroc.sese.asu.edu/archive/ (accessed April 04, 2019).

[21] Hapke, Bruce. "Bidirectional reflectance spectroscopy: 5. The coherent backscatter opposition effect and anisotropic scattering." *Icarus* 157.2 (2002): 523-534.

[22] KAMEI, Akihide, and Ryosuke NAKAMURA. "Light Scattering Properties of Small Bodies in the Solar System." *Journal of The Remote Sensing Society of Japan* 20.5 (2000): 563-575 (in Japanese).

[23] Wu, Weiren, et al. "Obstacle Recognition and Safe Area Selection Method in Soft Landing based on a Single Lunar Image." *Deep Space Exploration* 1.4

(2014): 262-268 (in Chinese).

[24] Gomi, Hiromi, et al. "Real-Time Recognition of Flat Areas for Lunar Landing Using Shape-from-Shading Technique." *Japan Society of Aeronautical Space Sciences* 52 (2004): 141-147 (in Japanese).

[25] Barron, Jonathan T., and Jitendra Malik. "High-frequency shape and albedo from shading using natural image statistics." *CVPR 2011*. IEEE, 2011.

[26] Grumpe, Arne, Fethi Belkhir, and Christian Wöhler. "Construction of lunar DEMs based on reflectance modelling." *Advances in Space Research* 53.12 (2014): 1735-1767.

[27] Barker, M. K., et al. "A new lunar digital elevation model from the Lunar Orbiter Laser Altimeter and SELENE Terrain Camera." *Icarus* 273 (2016): 346-355.

Acknowledgements

I would like to express my gratitude to all those people who helped me during these two years of master course.

Firstly, I would like to express my sincere gratitude to my supervisor, Professor Hashimoto Tatsuaki for his patience and continuous support during my master course. Professor Hashimoto gave us freedom to choose research topics that we are interested in, and offered lots of valuable suggestions. His incisive comments and constructive criticisms have contributed greatly to the completion of my two Rinko presentations and this graduation thesis.

I also want to thank my two tutors, Sano Shunta and Sakamoto Takuma. Mr. Sano helped me a lot with admission procedures and other necessary procedures for living in Japan. Mr. Sakamoto helped me a lot with my research, he helped check my grammar for Rinko materials written in Japanese and gave useful suggestions to make them more reasonable and easier to follow.

My sincere thanks also goes to everyone in the lab and JAXA staffs. The good atmosphere of this lab and the friendly people made my two-year master course fulfilling and happy. I am especially grateful to Professor Fukuda Seisuke for his patience and insightful comments towards my research. Also I want to thanks Mr. Yukio Yamamoto who is in charge of DARTS planetary for his help about the use of KAGAYA data.

Last, I would like to thank my parents, for their financial and spiritual support. This is the first time for me to live and study abroad for such long time, I have met many difficulties during these two years. But thanks to their consistent support and understanding, I would able to face and overcome all these difficulties and finish my Master course. Also thanks my friends who have been there for me every time I need help.